Title

Using Dark Fiber and Distributed Acoustic Sensing to Characterize a Geothermal System in the Imperial Valley, Southern California

Journal

Journal of Geophysical Research: Solid Earth, 128(3)

ISSN

2169-9313

Authors

Cheng, Feng

Ajo-Franklin, Jonathan B

Nayak, Avinash

et al.

Publication Date

2023-03-01

DOI

10.1029/2022jb025240

JGR Solid Earth

RESEARCH ARTICLE
10.1029/2022JB025240

Using Dark Fiber and Distributed Acoustic Sensing to Characterize a Geothermal System in the Imperial Valley, Southern California

Feng Cheng[1,2], Jonathan B. Ajo-Franklin[2,3], Avinash Nayak[3], Veronica Rodriguez Tribaldos[3], Robert Mellors[4], Patrick Dobson[3], and the Imperial Valley Dark Fiber Team[5]

[1]School of Earth Sciences, Zhejiang University, Hangzhou, China, [2]Department of Earth, Environmental, and Planetary Sciences, Rice University, Houston, TX, USA, [3]Lawrence Berkeley National Laboratory, Berkeley, CA, USA, [4]Institute of Geophysics and Planetary Physics, Scripps Institution of Oceanography, UC San Diego, La Jolla, CA, USA, [5]See Appendix A

Key Points:

- We utilize high-resolution ambient noise imaging to characterize a geothermal system using distributed acoustic sensing and dark fiber
- We develop a bin stacking technique to attenuate the effects of persistent local noise sources and enhance the retrieved empirical Green's functions
- We image a zone of high shear wave velocity beneath the Brawley geothermal field, which we interpret to be a zone of hydrothermal alteration

Supporting Information:

Supporting Information may be found in the online version of this article.

Correspondence to:

J. B. Ajo-Franklin,
ja62@rice.edu

Citation:

Cheng, F., Ajo-Franklin, J. B., Nayak, A., Tribaldos, V. R., Mellors, R., Dobson, P., & the Imperial Valley Dark Fiber Team (2023). Using dark fiber and distributed acoustic sensing to characterize a geothermal system in the Imperial Valley, Southern California. *Journal of Geophysical Research: Solid Earth*, *128*, e2022JB025240. https://doi.org/10.1029/2022JB025240

Received 26 JUL 2022
Accepted 25 FEB 2023

Author Contributions:

Conceptualization: Feng Cheng
Data curation: Feng Cheng
Formal analysis: Feng Cheng
Funding acquisition: Jonathan B. Ajo-Franklin
Investigation: Feng Cheng
Methodology: Feng Cheng
Project Administration: Jonathan B. Ajo-Franklin
Resources: Feng Cheng
Software: Feng Cheng

Abstract The Imperial Valley, CA, is a tectonically active transtensional basin located south of the Salton Sea; the area hosts numerous geothermal fields, including significant hidden hydrothermal resources without surface manifestations. Development of inexpensive, rugged, and highly sensitive exploration techniques for undiscovered geothermal systems is critical for accelerating geothermal power deployment as well as unlocking a low-carbon energy future. We present a case study utilizing distributed acoustic sensing (DAS) and ambient noise interferometry for geothermal reservoir imaging, utilizing unlit fiber-optic telecommunication infrastructure (dark fiber). The study exploits two days of passive DAS data acquired in early November 2020 over a ~28-km section of fiber from Calipatria, CA to Imperial, CA. We apply ambient noise interferometry to retrieve coherent signals from DAS records and develop a bin stacking technique to attenuate the effects from persistent localized noise sources and to enhance retrieval of coherent surface waves. As a result, we are able to obtain high-resolution two-dimensional (2D) S wave velocity (V_s) structure to 3 km depth, based on joint inversion of both the fundamental and higher overtones. We observe a previously unmapped high V_s and low V_p/V_s ratio feature beneath the Brawley geothermal system, which we interpret to be a zone of hydrothermal mineralization and lower porosity. This interpretation is consistent with a host of other measurements including surface heat flow, gravity anomalies, and available borehole wireline data. These results demonstrate the potential utility of DAS deployed on dark fiber for geothermal system exploration and characterization in the appropriate geological settings.

Plain Language Summary Geothermal resources are considered a valuable component of our global transition to a zero-emissions sustainable energy future. In the Imperial Valley, CA, three of the four producing geothermal fields have no active surface features. The development of inexpensive, rugged, and highly sensitive exploration techniques for undiscovered geothermal systems is a critical step in accelerating geothermal power discovery and deployment. We utilize a novel technology that converts ~28-km section of existing unused telecommunication fiber into seismic sensors (called distributed acoustic sensing, DAS) to characterize the subsurface geothermal resources. Ambient seismic noise data are recorded and processed to retrieve high quality coherent seismic waves after localized noise sources are attenuated. Our results reveal significant high-velocity anomalies beneath the Brawley Geothermal Field; these are coincident with observations from boreholes, heat flow, and gravity surveys which indicate hydrothermal alteration has a pronounced effect on the physical properties of the metamorphosed sediments.

1. Introduction

Geothermal energy is considered a key base-load resource for transitioning to a zero-emissions sustainable energy future (Sbrana et al., 2021). Geothermal energy currently accounts for only 0.4% of net electricity generation (~18.3 GW) in the United States (EIA, 2021). However, the U.S. Department of Energy has established an ambitious goal of supplying 60 GW of enhanced geothermal (EGS) and expanded hydrothermal by 2050 (GTO, 2022). Accomplishing these goals will require significant advances in exploration, reservoir characterization, and resource development. Studies assessing the electric power production potential from US moderate-to-high temperature geothermal resources estimate that the power production potential from undiscovered geothermal resources is more than three times the estimated potential from identified geothermal systems (C. Williams

Supervision: Jonathan B. Ajo-Franklin
Validation: Feng Cheng
Visualization: Feng Cheng
Writing – original draft: Feng Cheng
Writing – review & editing: Feng Cheng, Jonathan B. Ajo-Franklin, Avinash Nayak, Veronica Rodriguez Tribaldos, Robert Mellors, Patrick Dobson

et al., 2008). A significant portion (~30%) of the estimated undiscovered resource in the US is predicted to occur within the Imperial Valley (C. Williams et al., 2009). Development of improved exploration strategies for undiscovered geothermal systems is critical for accelerating geothermal power deployment (Dobson, 2016; C. Williams et al., 2009).

Active hydrothermal systems are often associated with measurable differences in physical properties (e.g., high heat flow, low electrical resistivity, elevated density, and attenuation of high frequency elastic waves). As a result, geophysical methods can play a key role in geothermal exploration (e.g., Combs, 1978; Flóvenz & Saemundsson, 1993; Santos & Rivas, 2009; Thanassoulas, 1991; Zucca et al., 1994). For example, heat flow anomalies, derived from temperature measurements in shallow boreholes, can be used to locate and outline potential geothermal fields (Burton-Johnson et al., 2020; Fahnestock et al., 2001; Kratt et al., 2008; Zehner et al., 2012). Gravity surveys can be used to study the depth of fill in intermontaine valleys, locate intrusive masses of rock and delineate geothermal features (Atef et al., 2016; Guglielmetti & Moscariello, 2021). A combination of resistivity profiles, derived from active or passive electromagnetic (EM) surveys, and heat flow measurements from temperature gradient wells are often used to search for zones likely to host permeable geothermal reservoirs sealed with an overlying clay cap (Anderson et al., 2000; Gao et al., 2018; Munoz, 2014). Active-source seismic reflection profiles can be used to identify faults, which may facilitate flow, in hot sedimentary systems using reflection offsets, as well as image basement contacts and verify structures related to tectonic processes relevant to geothermal system development (Brogi et al., 2005; Lüschen et al., 2011; McGuire et al., 2015). Lastly, passive microseismic surveys are widely used for studying slip on seismogenic faults, which may create and maintain permeability (Combs & Hadley, 1977; Lellouch et al., 2020; Ward, 1972). However, considering the limitations of these different approaches, suites of methods are typically used in concert to verify proposed system location, conditions, and associated structures before exploratory wells are drilled (Ars et al., 2019; Soyer et al., 2018).

Compared to relatively expensive active-source seismic methods, ambient noise interferometry can be a cost-effective imaging approach, valuable for both characterization and long-term monitoring. Following the pioneering work of Campillo and Paul (2003), ambient noise interferometry can be used to estimate an empirical Green's function (EGF) between two receivers by cross-correlating the ambient seismic wavefield (Behm et al., 2019; Bensen et al., 2007; Cheng et al., 2016, 2018; Fichtner et al., 2020; Nakata et al., 2015; Shapiro & Campillo, 2004; Snieder, 2004; Snieder et al., 2009; Wapenaar, 2004). In recent years, ambient noise interferometry techniques have found a variety of applications for geothermal reservoir imaging, often leveraging dense arrays of nodal (i.e., passive autonomous) seismometers (e.g., Cheng, Xia, Ajo-Franklin, et al., 2021; Lehujeur et al., 2018; Martins et al., 2019, 2020; Planès et al., 2020; Spica et al., 2018; Zhou et al., 2021). Recorded EGFs are often rich in surface wave energy, hence the most commonly retrieved physical property from ambient noise studies are shear wave velocities estimated using surface wave tomography methods.

Currently, there are still large portions of western basins in the U.S. that are relevant to geothermal energy production but poorly mapped using classical high-resolution seismic methods. This is due to the high costs of active seismic surveys and the lack of availability of "Large-N" passive seismic datasets required for ambient noise imaging. These factors likely result in both missed prospects as well as limitations in our understanding of regional geological frameworks relevant to geothermal prospecting.

Distributed fiber optic sensing is a family of techniques that utilizes standard optical fibers to make measurements of local physical parameters including temperature (Tyler et al., 2009), static strain (Masoudi & Newson, 2016), and most recently low amplitude dynamic strain or strain rate (Lindsey & Martin, 2021). The last approach, referred to as distributed acoustic sensing (DAS), is an emerging technology that repurposes a fiber-optic cable as a dense array of seismic sensors and in some environments is transforming seismic acquisition (Ajo-Franklin et al., 2019; Cheng, Chi, et al., 2021, 2022; Daley et al., 2013; Dou et al., 2017; Lindsey et al., 2017; Martin et al., 2021; Zhan, 2020). DAS utilizes laser pulses to interferometrically measure minute extensional strains (or strain rates) over spatially continuous intervals along an optical fiber (Hartog, 2017), and has advantages of fine spatial resolutions down to the meter scale with linear extents from tens to hundreds of km, and broad bandwidth from the kHz range to quasi-static depending on interrogator unit and measurement parameters (Lindsey et al., 2020; Paitz et al., 2021). DAS has been successfully used for urban near-surface characterization (Ajo-Franklin et al., 2019; Dou et al., 2017; Fang et al., 2020), monitoring of unconventional reservoirs (Cheng et al., 2021; Daley et al., 2013; Jin & Roy, 2017), glacial deformation (Booth et al., 2020; Walter et al., 2020), and ocean dynamics (Cheng, Chi, et al., 2021; Lindsey et al., 2019; E. F. Williams et al., 2021; Viens et al., 2022).

Recently, several DAS-related feasibility studies have been conducted to characterize geothermal reservoirs (e.g., Chalari et al., 2019; Chang & Nakata, 2022; Feigl & Parker, 2019; Feigl & Team, 2017; Kasahara et al., 2020; Lellouch et al., 2021; Schölderle et al., 2021).

In the Imperial Valley, CA, there are three producing geothermal systems that have no active surface thermal features and additional undiscovered resources likely exist in the region (e.g., C. Williams et al., 2009). In this study we investigate the potential of high-resolution ambient noise imaging, using DAS data acquired on existing unused telecommunications fiber, to image geothermal reservoir structure. We briefly summarize the acquisition and the main characteristics of ambient seismic noise records obtained from the ∼28-km Imperial Valley Dark Fiber (IVDF) DAS array that runs along a portion of Imperial Valley, CA, and crosses the producing Brawley geothermal field; a detailed overview of the acquisition and associated metadata was recently presented in Ajo-Franklin et al. (2022). We then extract high-quality Rayleigh waves based on ambient noise interferometry, and apply surface wave inversion across the profile to generate a two-dimensional (2-D) S wave velocity model. The resulting image identifies a zone of high V_s closely correlated with the Brawley heat flow anomaly. We hypothesize that the imaged feature is due to a zone of hydrothermal mineralization at the core of the Brawley geothermal field, which has resulted in significant reduction in porosity. We conclude by attempting to verify this hypothesis using secondary datasets including regional velocity models, existing wireline logs, gravity measurements, and heat flow data. Our results demonstrate the feasibility of such passive DAS surveys for detecting and characterizing structures relevant to geothermal systems at the basin scale.

2. Area and Data

The Imperial Valley, south of the Salton Sea, is part of the landward extension of the Gulf of California, within a broad, structural trough (referred to as the Salton Trough) partly filled with late Tertiary deltaic sediments which are in turn covered by Quaternary alluvium and lacustrine deposits (Jackson, 1981). The Salton Trough is a tectonically active rift basin located at the southern terminus of the San Andreas Fault system as it steps over into the continental transitional zone between the North American and Pacific Plates (Kaspereit et al., 2016). The transition from transform faulting to rifting results in a series of smaller-scale pull-apart basins of different sizes that connect right-stepping, strike-slip faults that strike generally northwest (Elders et al., 1972; Fuis et al., 1982; Hill, 1977; Hill et al., 1975; Johnson & Hadley, 1976). This pattern of faulting forms in transtensional shear zones where there are structures related to both strike-slip and extension. Major faults (red lines in Figure 1a) in the region include the Imperial Fault (IF), the Superstition Hills Fault (SHF), the Superstition Mountain Fault (SMF) and the Brawley Fault (BF, we use the Brawley fault as mapped by Hill et al. (1975) and Jackson (1981)). The southeast end of the San Andreas Fault is linked to the northwest end of the Imperial Fault by a band of seismicity referred to as the Brawley Seismic Zone (outlined by the orange line in Figure 1a).

Within the Salton trough, these tectonic forces are currently active and allow mantle-sourced magmas to intrude into the shallower sediments, which are evidenced by the presence of young rhyolitic domes along the southern shore of the Salton Sea and the intersection of buried rhyolitic domes in a number of geothermal wells in the Salton Sea Geothermal Field (e.g., Herzig & Jacobs, 1994; Hulen & Pulka, 2001; Schmitt & Hulen, 2008). Past studies have inferred igneous intrusion at depth due to the existence of potential field anomalies (both gravity and magnetic), high seismic velocities, and a localized zone of elevated heat flow; these geophysical signatures are aligned with Quaternary volcanism visible in surface exposures on the southern shore of the Salton Sea (Biehler, 1964; Elders et al., 1972; Larson et al., 1968; Lomnitz et al., 1970). Current regional thermal models hypothesize that these intrusive features provide a heat source for hydrothermal activity and drive sediment alteration (McGuire et al., 2015). The thick deltaic sediment stack filling the basin contains geothermal brines in some locations, referred to as known geothermal resource areas (KGRA, highlighted with green polygons in Figure 1a): Salton Sea Geothermal Field (SSGF), Brawley Geothermal Field (BGF), East Mesa Geothermal Field (EMGF) and Heber Geothermal Field (HGF); there are additional KGRAs in the area (such as Westmorland, Glamis, and Dunes) that have yet to be developed.

Local seismicity and earthquake focal mechanisms across the area have been extensively studied (Brodsky & Lajoie, 2013; Hauksson et al., 2013; Hill et al., 1975; Lin et al., 2007; Lohman & McGuire, 2007; Marone et al., 1991). Historical seismicity has been characterized by narrow zones of right lateral events extending between the Brawley and the Imperial faults within the Brawley Seismic Zone, and a broader zone of right lateral activity along the San Jacinto Fault. Seismic activity was also observed at the Salton Sea and Brawley geothermal

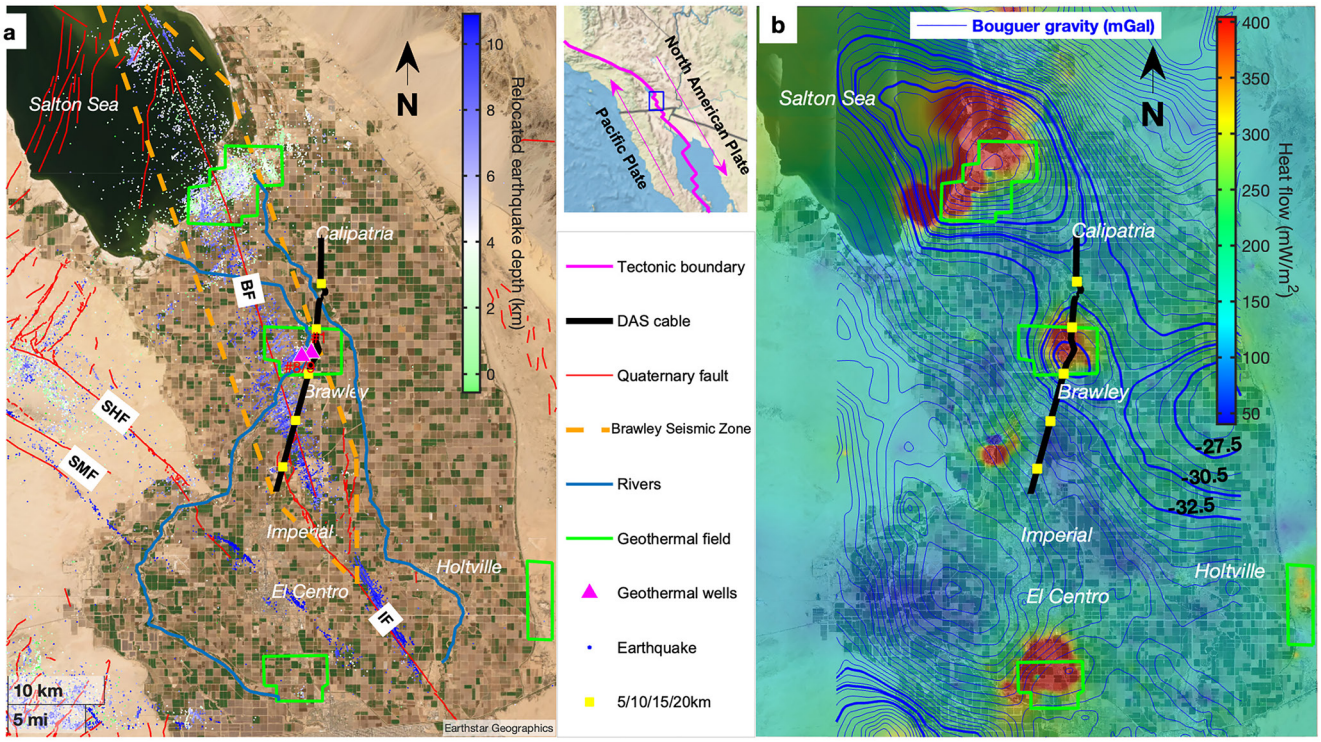

Figure 1. Site overview of the Imperial Valley dark fiber experiment. (a) Maps of the Imperial Valley with distributed acoustic sensing cable array (black line), Quaternary faults (red lines), Brawley seismic zone (orange dash-line polygon), rivers (Alamo River and New River, steelblue lines), geothermal fields (green polygons), geothermal wells (magenta triangles, #1, #8, and #9) discussed in this paper, and historical earthquakes from 1981 to 2019 (blue-to-green colored dots). The colors of earthquakes are coded by the relocated depths (Hauksson et al., 2012). Five yellow squares mark the cable length at 5/10/15/20/25 km locations referring to the north starting end. Major faults in the region are indicated by capital letters as follows: Imperial Fault (IF), Superstition Hills Fault (SHF), Superstition Mountain Fault (SMF) and Brawley Fault (BF). (b). Heat flow map (C. Williams et al., 2007, 2008) of the Imperial valley area overlaying with Bouguer gravity contours (blue lines) (Biehler, 1964, 1971).

fields, which lie on the Brawley fault, and at the Heber geothermal field near the extension of the San Jacinto Fault. In contrast, the Glamis and Dunes geothermal areas and the East Mesa geothermal field have experienced low levels of seismicity in the past. These observations are consistent with the historical earthquake catalog (green-to-blue scatters in Figure 1a) relocated by Hauksson et al. (2012).

Past efforts to locate hidden geothermal systems in the Imperial Valley have yielded an unusually detailed map of regional heat flow (C. Williams et al., 2007, 2008). Figure 1b clearly shows that the SSGF geothermal system and three previously hidden geothermal systems (BGF, EMGF, and HGF), highlighted with green polygons, are visible as areas of elevated heat flow with local values >350 mW/m^2. The average heat flow in the region is roughly twice as large as the national average heat flow (Lachenbruch & Sass, 1973). The visibility of thermal anomalies beyond previously mapped KGRAs suggests that significant untapped resources may still exist within the basin (Dobson, 2016; C. Williams et al., 2007, 2008). The blue contours in Figure 1b show Bouguer gravity data, acquired by Biehler (1964, 1971), overlain on the heat flow map. As can be seen, the positive Bouguer anomaly is aligned with the basin axis, north-northwest; observed gravity highs typically coincide with zones of higher heat flow and known hydrothermal systems.

Our experiment, described in detail in Ajo-Franklin et al. (2022), utilized an existing fiber-optic telecommunication cable (dark fiber) starting in Calipatria, CA, running through Brawley and Imperial CA, and then turning West at El Centro, terminating in Plaster City. The total path length (~65 km) is too long for the DAS interrogator unit used in this experiment to fully probe; only the first ~28-km section, the black line in Figure 1, is utilized with a roughly straight path crossing the previously hidden geothermal resources of the Brawley Geothermal Field and the complex transition zone, the Brawley Seismic Zone, where the Brawley Fault lies. The fiber cable was entirely subsurface over this section; while detailed engineering drawings were not available from the provider, we believe the bulk of the fiber was trenched and housed in PVC conduit.

The IU data collection system was installed on 9 November 2020 in an Intermediate Light Amplification (ILA) hut in Calipatria, CA. To build a calibrated network geometry, the DAS channel locations across the array were updated by tap tests, where an operator uses a hammer to create a vibration at a known location like the fiber surface marker to provide the interpreter a known point for channel index along the fiber profile. For acquisition, we utilized an iDAS v2 IU (Silixa LLC) which wrote onto a local RAID storage system (QNAP). Data were acquired at a fixed 10 m gauge length in strain-rate with a 2 kHz laser pulse rate and a 500 Hz sampling rate. Ambient noise data were continuously recorded at 4 m channel interval across the ∼28 km (total 6,912 channels) dark fiber (single-mode SMF-28) from 10 November 2020 till the spring of 2022. Continuous records were stored in 1-min blocks in HDF-5 format; each record was approximately 415 MB in size.

After the first round of data retrieval in the spring of 2021, we obtained close to 4 months of continuous data (approximately 65T in size) from 10 November 2020 to 8 March 2021. In this study, we utilize only the first two days of recording to evaluate the feasibility of using DAS-based ambient noise data for high-resolution geothermal reservoir mapping. Complete details about experiment, installation information, earthquake observations as well as metadata are provided in Ajo-Franklin et al. (2022).

3. Methods

3.1. Noise Characteristics

Figure 2a shows a sample time-domain ambient noise record from the DAS fiber with several identified seismic signatures associated with anthropogenic sources. Noise characteristics vary significantly across the profile. The signatures of moving vehicles are visible with linear moveouts, a common observation in urbanized areas on both dense nodal (Cheng et al., 2018, 2019) and DAS arrays (Ajo-Franklin et al., 2019; Rodríguez Tribaldos et al., 2021; Wang et al., 2020). A series of persistent noise sources are also observed across the DAS array, visible as stationary surface wave generators and highlighted by the dashed lines in Figure 2a. Examples include agricultural and transport infrastructure, such as the grain silos and a loading facility, located at approximately 0.9 km along the array, an overpass excited in resonance around 15 km, and an agriculture products wholesale facility close to 16 km. These powerful noise sources generate coherent surface waves visible propagating over multiple km; however, the persistent localized sources with strong spatial consistency (almost zero moveout indicated by the vertical dashed lines) will produce non-negligible spurious signals superimposed on empirical Green's functions (EGFs) during ambient noise interferometry, an issue which will be discussed in later sections. Finally, toward the southern end of the array, increasing noise levels are observed due to optical losses (Cedilnik et al., 2019; Waagaard et al., 2021) as well as the lack of traffic activities in the southern cropland area.

An average of 1 min power spectrum (Figure 2b) of the first 2 days of DAS ambient noise data along the cable shows that the dominant noise band is between 1 and 20 Hz, a typical spectra for anthropogenic noise sources (Cheng et al., 2019; Groos & Ritter, 2009; Zhu & Stensrud, 2019). The variable spectrum at the southern end of the array indicates the lack of anthropogenic signals. It is worth mentioning that the slightly quieter interior array section with dominant lower-frequency spectrum is located near the BGF. In this zone, and in urban areas, we also observe the existence of many discrete frequencies (e.g., 10, 20, and 30 Hz) that might be due to power line subharmonics coupled into an unknown mechanical sources. Due to the all-optical nature of DAS, they are likely not inductively coupled. These frequencies are ignored in our low frequency (<5 Hz) DAS seismic imaging study but might be relevant for near-surface ambient noise investigations.

3.2. Ambient Noise Interferometry

Ambient noise interferometry is a family of processing approaches that attempts to reconstruct the Green's function between two receivers by cross-correlating the random seismic wavefields (i.e., noise) recorded at both locations. Assuming a homogeneous distribution of random noise sources, the cross-correlation of recorded displacement components at sensors A and B can be written as (Gouedard et al., 2008; Lobkis & Weaver, 2001; Snieder, 2004)

$$\frac{d}{d\tau}C_{AB}(\tau) = -\frac{\sigma^2}{4a}(G_{AB}(\tau) - G_{AB}(-\tau)) \quad (1)$$

where, C_{AB} is the time domain cross-correlation between the displacement at the two receivers A and B, G_{AB} is the Green's function between A and B, σ is the variance of the ambient noise field and a is a small attenuation coefficient. Despite the known challenges in retrieval of empirical Green's functions (EGFs), ambient

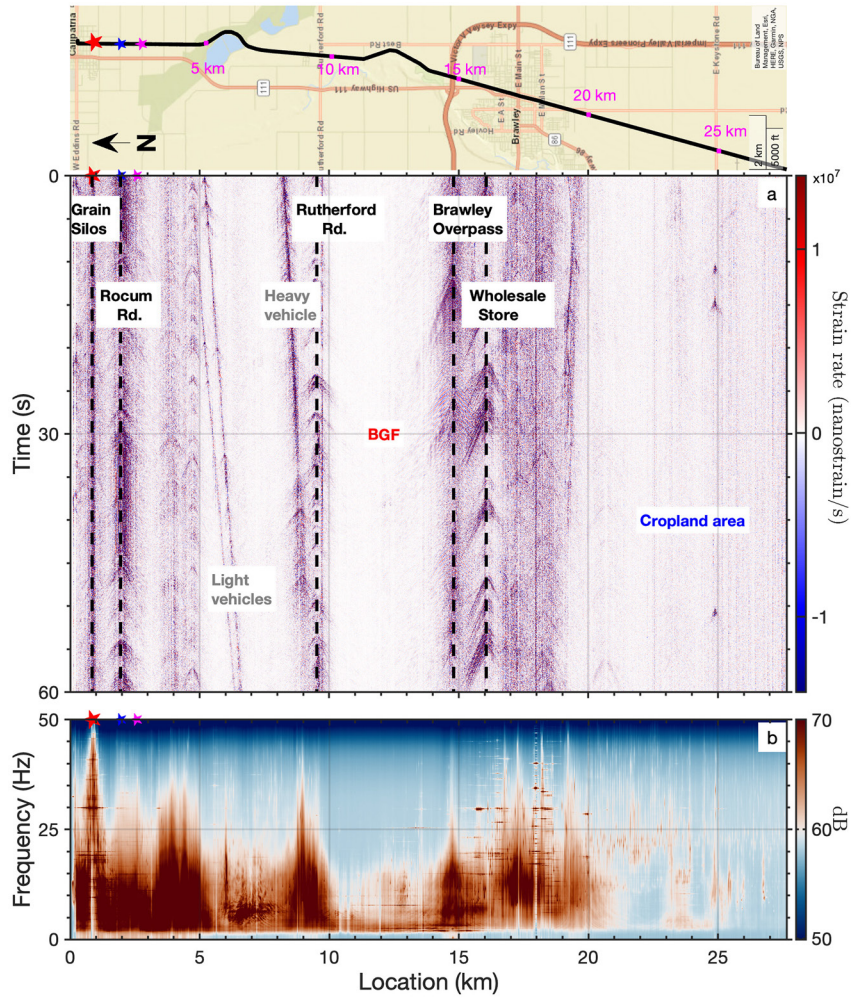

Figure 2. Observations of ambient noise on a ~28 km distributed acoustic sensing array. Panel (a) 60-s-long ambient noise record in strain-rate (unit, nanostrain/s) with seismic signatures from moving vehicles and persistent localized sources, like factories, crossing roads, Brawley overpass, and Brawley Airport. A rotated street map on the top of (a) shows the main infrastructures crossing the cable. Panel (b) 2-day averaged spectrum of the noise along the cable. Three colored stars represent the detected persistent localized sources, like grain silos (the red star) and crossing roads (the blue stars).

noise interferometry has been adapted to extract EGFs from surface DAS array using plane-wave theory (Dou et al., 2017; Martin et al., 2017, 2021). Generalized strain (DAS) interferometry equations have also been presented in the form of a representation theorem (Paitz et al., 2019). More recently, hybrid EGFs for strain-rate and velocity/strain-rate cross-correlations were introduced by Nayak and Ajo-Franklin et al. (2021) expanding the application of ambient noise seismology for networks including both DAS and inertial sensors.

Using ambient noise interferometry, we generated empirical Green's functions from the passive DAS data recorded on the Imperial Valley dark fiber array. Considering the large array size and high temporal sampling, interferometric processing was not applied to the raw data. We initially decimated the data set to 100 Hz in the time domain after applying a FIR anti-aliasing low-pass filter; this step was followed by sequential spatial median stacking with a five channel window, which transformed the data set from 6,912 channels ($\Delta X = 4$ m) to 1,382 channels ($\Delta X = 20$ m). As a result of these steps, each 1 min noise record was reduced in size from 415 Mb to ~17 Mb, simplifying downstream analysis.

We then applied a classical ambient noise data preprocessing workflow (e.g., Bensen et al., 2007; Cheng et al., 2015; Cheng, Xia, Ajo-Franklin, et al., 2021) to the continuous DAS data set (2 days) by processing each 1 min data block in native recording units (strain rate). Preprocessing steps included mean and trend removal to minimize the impact of drift as well as a 5% window Hanning taper applied to both ends of the time series.

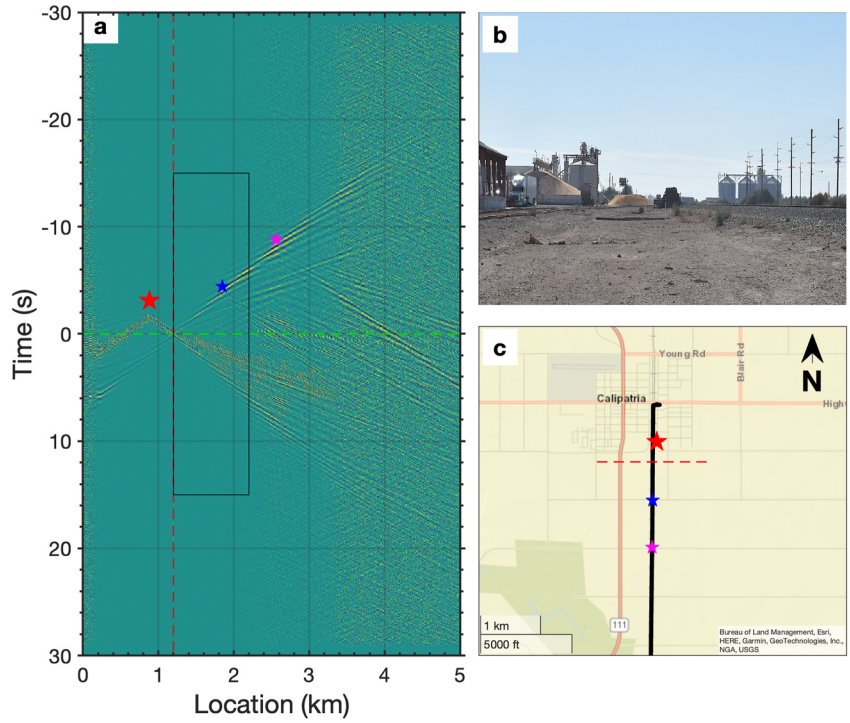

Figure 3. Example of the effect from persistent localized source. (a) Empirical Green's function gather with virtual source at 1.2 km location (indicated by the red dashed line). The colored stars indicate the persistent localized sources, from the working grain silo (red star), Yocum Rd (blue star) and Albright Rd (magenta star), which have been notated on the raw waveform map. Panel (b) shows the site photo of the grain silo beside the cable line as indicated by the red star on (c). The street map on (c) shows Yocum Rd and Albright Rd crossing the fiber-optic cable (the black line). The red dashed line on (c) shows the location of the virtual source on the cable. Seismic signature of the grain silo is significantly different to that of the crossing roads and shows dominant higher frequency components.

These steps were followed by temporal and spectral normalization. The temporal normalization was performed by applying a 5% window running absolute mean filter. This step, advocated by Bensen et al. (2007), effectively equalizes nonstationary noise sources including earthquakes and large amplitude transient noise events in the record. We utilize a frequency domain whitening approach to improve EGF bandwidth; the weighting function exploits the smoothed amplitude of complex Fourier spectrum of each record (e.g., Bensen et al., 2007; Cheng, Chi, et al., 2021).

To extract EGFs from the preprocessed ambient noise data set, we utilized the cross-coherence algorithm which consists of cross-correlation followed by spectral whitening (Nakata et al., 2011; Prieto et al., 2009; Schuster et al., 2004). Following Cheng, Xia, Ajo-Franklin, et al. (2021), the cross-coherence algorithm has advantages over the cross-correlation algorithm for mitigating pseudo-arrivals associated with spectral spikes and improving the signal-to-noise ratio (SNR) of the resulting EGFs. After cross-coherence, we employ phase-weighted stacking (PWS), a technique that emphasizes contributions of coherent components to the stack and degrades weights of incoherent noise that do not share the same instantaneous phase, on 2 days of EGFs to boost coherent signals (Schimmel & Paulssen, 1997; Schimmel et al., 2011; Ventosa et al., 2017).

In the case of this data set, special attention was paid to the effects of persistent localized noise sources, several of which are distributed across our array as discussed previously. Figure 3a displays an example of an extracted EGF gather after 2 days of phase-weighted stacking with a virtual source at 1.2 km location (indicated by the red dashed line). Coherent signals are observed as far as ~5 km offset range. Superimposed are three two-sided linear events which radiate from sources at 0.9, 1.8, and 2.6 km as highlighted with colored stars:

1. The northernmost feature is identified as persistent noise from a grain silo complex; Figure 3b shows a photograph of the site where vibrations are sufficiently strong to be felt by humans at a distance. High-frequency energy can also be observed on the averaged noise spectrum shown in Figure 2b.

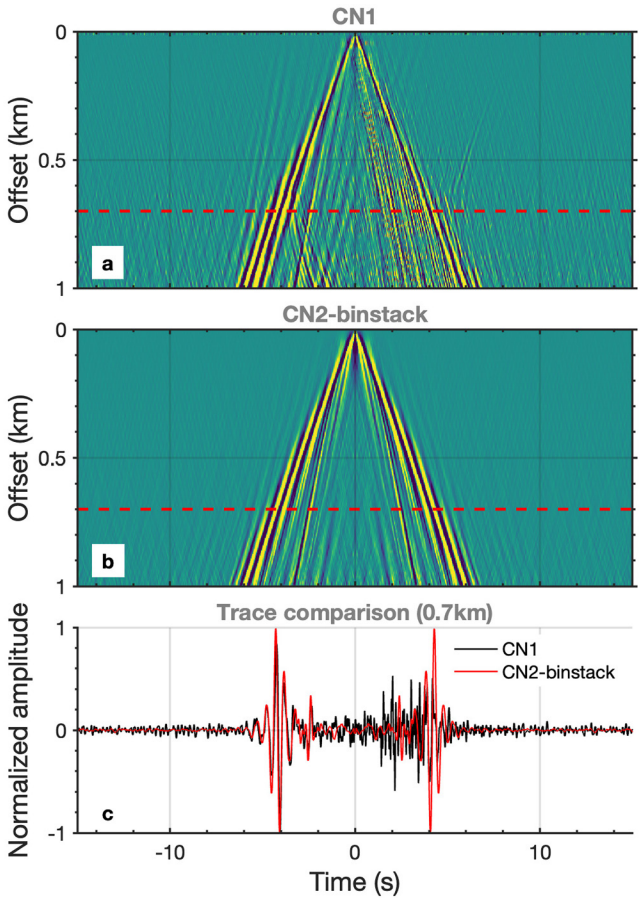

Figure 4. Performance of the bin stacking strategy. (a) The CN1 shot gather with the first channel as virtual source and the other N channels as virtual receivers (highlighted by the black box in Figure 3a). (b) The bin stacked shot gather with every channel as virtual source and the channels behind the virtual sources as virtual receivers. (c) Single trace comparison between CN1 (black) and CN2 bin stacking (red) shot gather at offset 0.7 km (highlighted by the red dashed line in (a and b)).

2. The other two dominant events are identified as source effects from roads crossing the fiber as indicated by the blue and magenta stars on the street map (Figure 3c). Compared with the energy from the grain silos, events from the persistent traffic noise usually show relatively lower frequencies and lower velocities with smaller moveouts.

It is worth mentioning that the term "persistent localized source" in this work mainly indicates that the source is spatially persistent and temporally frequent, breaking the assumptions of randomly distributed noise sources underlying much of the theory of ambient noise imaging. Studies focused on persistent localized noise sources have gained increasing attention with recent work ranging from source localization (Zeng & Ni, 2010) to seismic monitoring (Dales et al., 2017). However, these studies are usually limited by the sparse spatial sampling available with conventional seismic networks; DAS offers an alternative approach to study and utilize these persistent localized sources for potential seismic imaging and monitoring (Song et al., 2021; E. F. Williams et al., 2021; Zeng et al., 2017).

Other recent studies have attempted to utilize these spurious events for structural seismic imaging (Yang et al., 2022). However, we believe that these events are source-related rather than structure-related according to our observations; for example, these events are usually located around the traffic intersections and disappear during the late evening hours. Our focus is on strategies to attenuate these persistent localized sources to improve the quality of conventional ambient noise imaging.

We developed a simple processing workflow to reduce these spurious events associated with persistent localized noise sources and to enhance the SNRs of the resulting EGF. For conventional ambient noise imaging utilizing linear arrays and multichannel analysis of surface waves (MASW) technique, a roll-along strategy, commonly applied in active-source surface wave surveys (Mi et al., 2017; Park, 2005; Xia et al., 2009), is often utilized. In this approach, the array is separated into a series of subarrays that are "rolled" along the profile to image subsurface lateral variations. In this workflow, each subarray contains only one virtual-source cross-correlation/coherence gather with the first trace selected as the virtual-source (we refer to these as CN1 virtual-source gather) to ensure the uniform spatial coverage. In this study, CN1 virtual-source gathers are replaced by bin-offset stacked CN2 virtual-source gathers for each subarray where $C_N^2 = 1 + 2 + \ldots n - 1$ and n is the number of traces in each subarray. Here CN1 and CN2 are defined after the basic combinatorics formula. Bin-offset stacks simply stack all EGF source-receiver pairs that have the same spatial offset into a single super-gather. Bin-offset stacking techniques have been used for signal enhancement for 2-dimensional (2D) dense arrays (Cheng, Xia, Ajo-Franklin, et al., 2021; Nakata et al., 2015; Zeng et al., 2021); we apply this technique to our dense 1-dimensional (1D) DAS array. In our approach, cross-coherence functions are first extracted for all possible inter-station pairs (CN2) after 2 days of PWS stacking. The resulting gathers are then spatially averaged using bin-offset stacking to generate an enhanced virtual-source gather. This binning approach increases the quality of the retrieved EGFs, particularly for cross-coherence pairs with small offsets, and tends to mitigate artifacts due to persistent noise sources and local lateral heterogeneity within each subarray. As a result, the stacked EGFs are more uniform, and generate more consistent dispersion curves that are more effectively inverted using traditional surface wave analysis algorithms. However, as one would expect, some degree of lateral resolution is lost in the stacking process.

Figure 4 shows a typical example of the performance of bin stacking. Compared with the CN1 virtual-source gather (Figure 4a), the CN2 bin stacked virtual-source gather (Figure 4b) has been significantly improved with attenuation of spurious arrivals associated with persistent localized sources and SNR enhancement as indicated by the trace-by-trace comparison shown in Figure 4c. The interval of the offset bins used in this work is 20 m, similar to the spatial sampling of the decimated data set.

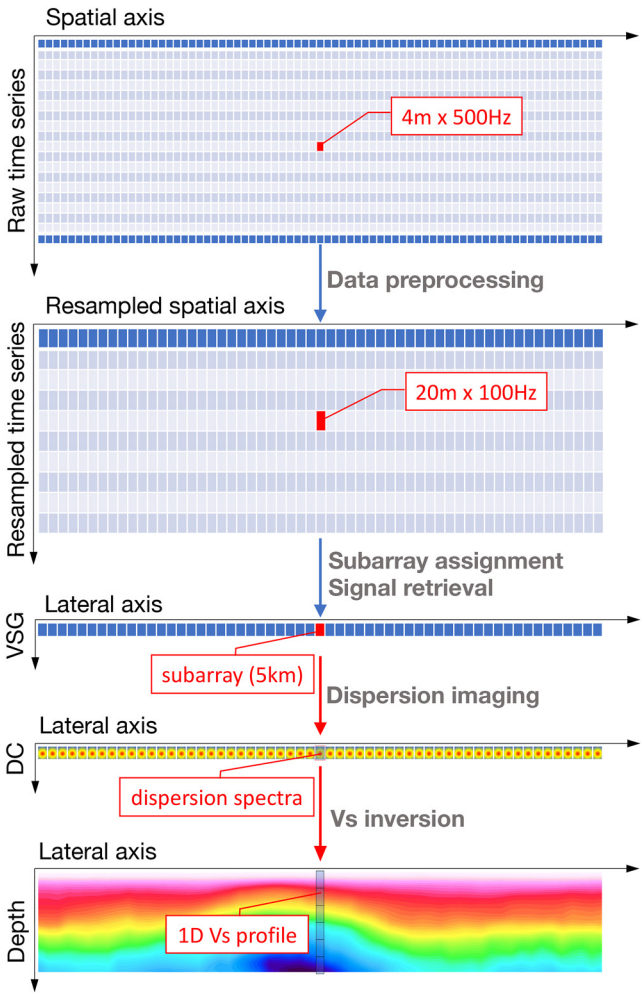

Figure 5. Workflow of distributed acoustic sensing ambient noise imaging including preprocessing, virtual source gather (VSG) generation, dispersion curve (DC) measurement, and V_s inversion. The raw ambient noise data are sampled in 4 m spatial interval and 500 Hz sampling rate; the decimated data are resampled in 20 m spatial interval and 100 Hz sampling rate. The virtual-source gather is constructed by bin stacking the retrieved CN2 EGFs within one subarray (5 km), and used for dispersion spectra imaging as well as 1D V_s profile inversion. See Figure S1 in Supporting Information S1 for details of the data processing flow chart.

3.3. Surface Wave Imaging

As described above, a MASW roll-along strategy is implemented for ambient noise imaging. In order to ensure sufficient imaging depth and lateral resolution for geothermal reservoir characterization, a 5-km-subarray was selected to allow observations of surface waves with sufficient wavelengths for constraining properties at a depth of ~3 km (Foti et al., 2018; Xia et al., 2006). Subarrays roll along the DAS cable with a coverage overlap of 80% to ensure continuity of lateral variations beneath the DAS array. In total, we obtain 57 subarrays across the DAS cable; for each subarray the enhanced virtual-source gather after bin stacking is analyzed for dispersion imaging and subsequent 1D shear wave velocity (V_s) inversion. An integrated workflow of DAS ambient noise imaging developed for this study is presented in Figure 5, and consists of five steps:

1. Data preprocessing which decimates the data matrices and normalizes the time series (both temporal and spectral);
2. Subarray assignment which separates the whole DAS array into a series of short subarray targets under consideration of both spatial coverage and lateral resolution;
3. Interferometric processing and stacking that generates one enhanced virtual-source gather for each subarray after bin stacking;
4. Dispersion analysis based on the obtained virtual-source gather for each subarray;
5. V_s inversion, which constructs a series of 1D V_s profiles for all subarrays and aligns them along the cable to build a pseudo-2D velocity structure.

Surface wave dispersion analysis is conducted on each virtual-source gather by applying an improved frequency domain slant-stacking algorithm (Cheng, Xia, Zhang, et al., 2021), which employs a phase-weighted stacking technique to enhance spatial coherency during dispersion measurement. Figure 6 shows a typical example of the DAS-based surface wave retrieval (a) and dispersion image (b) at location ~22 km. Clear Rayleigh waves with apparent velocities varying between 200 and 800 m/s are visible on the enhanced virtual-source gather after bin stacking, without interference from spurious arrivals associated with persistent localized sources. It is worth mentioning that our surface radial-radial cross-correlation is not sensitive to Love waves because DAS is single-component sensing method and mainly responds to waves that induce an extensional strain across the length of the fiber (Martin et al., 2021). Higher overtones are clearly identified on the high-resolution dispersion spectrum. For accurate dispersion curve picking, we limit the target zone using the effective wavenumber range or Nyquist limits defined by $k_{\min} = 1/L$ (L, array length 5 km) and $k_{\max} = 1/dx$ (dx, spatial interval 20 m) as indicated by the blue dashed lines on Figure 6b. Based on the enhanced surface wave shot gather and the high-resolution dispersion imaging technique, dispersion curves for multiple modes are manually picked across the DAS profile (see Figure S2 in Supporting Information S1 for all the picked curves in supporting information). Note that the offset information has been calibrated by tap tests results rather than the fixed channel interval, so that the geometry across the two curved sections around 6 and 12 km locations will not impact phase velocity estimation; considering the curved sections are only around 2 km width, the weak curvature effect could be negligible after the spatial average of the bin stacking procedure.

To extract 1D V_s profile for each subarray, we simultaneously invert the multimode Rayleigh wave dispersion curves by using a neighborhood algorithm (NA) as implemented in the Geopsy package, which tends to be less sensitive to the initial model (Wathelet et al., 2004). We initialize the V_s model based on the picked fundamental-mode dispersion curves by following the empirical formula described in Xia et al. (1999),

$$vs_i = cr(f_i)/\alpha, \quad \alpha = 0.88, \quad i = 1 \ldots m \tag{2a}$$

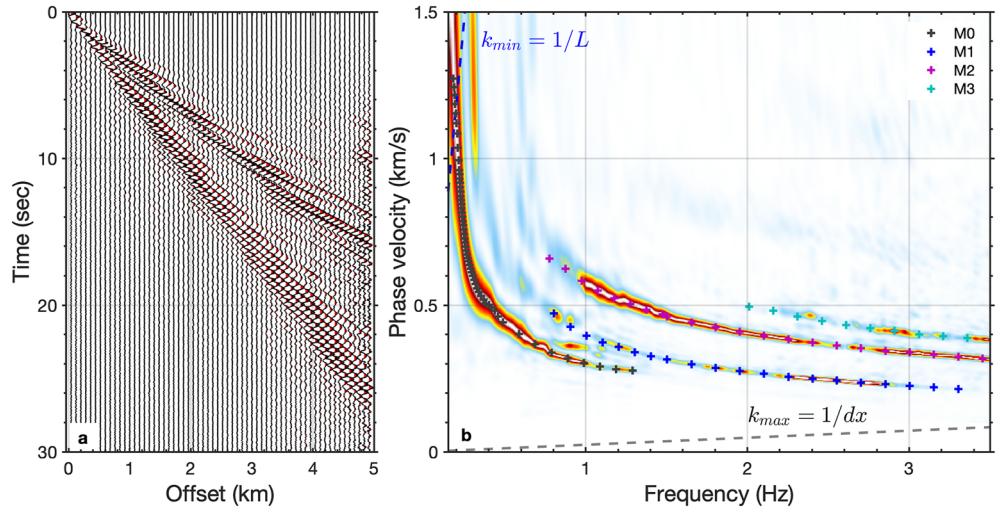

Figure 6. Distributed acoustic sensing-based surface wave retrieval and dispersion analysis. Panels (a and b) show the extracted Rayleigh wave shot gather after bin stacking and the corresponding dispersion measurement with multiple modes identified and picked. The blue dashed lines indicate the minimum wavenumber defined by $k_{\min} = 1/L$ (L, array length) and the maximum wavenumber defined by $k_{\max} = 1/dx$ (dx, spatial interval).

$$d_i = vs_i / f_i * \beta, \quad \beta = 0.63 \tag{2b}$$

where, $cr(f_i)$ indicates the picked dispersion curve at frequency f_i; m is the number of the picks; vs_i and d_i denote the appropriated shear wave velocity and the corresponding depth. Equation 2b depicts an empirical velocity-depth profile directly converted from the picked phase-velocity dispersion curve.

Our starting earth model pool is initiated with weak (±50% parametric perturbations) bounds based on the defined 14-layer initial V_s model; considering that the phase-velocity dispersion curve is less sensitive to the density and P wave velocity (V_p) values compared to the target V_s model, density is treated as a free parameter with a constant initial value (2.0 g/cm^3), and V_p is linked to V_s during the inversion with a limited Poisson ratio range from 0.4 to 0.45. The number of layers is fixed as defined in the initial model, and the thickness of each layer is flexible with ±50% perturbations. For each subarray, we invert the multimode dispersion curves with three independent runs of the inversion process. Each run retains 2500 models for target search. To reduce potential uncertainties within the neighborhood algorithm as well as to avoid overfitting, we extract the optimal V_s model with a misfit-weighted mean model rather than the individual model with the smallest/best misfit: we select the first 100 models with smallest misfit values from all retained models of all three runs. We then perform a weighted average of this family of 100 models using their corresponding misfits

$$vs = \sum_{j}^{N} vs_j * (1 - \varepsilon_j) / \sum_{j}^{N} (1 - \varepsilon_j) \tag{3}$$

where, vs_j indicates the *jth* model of the selected $N = 100$ models; ε_j is the misfit of the *jth* model, thus $1 - \varepsilon_j$ indicates the corresponding confidence degree of this model; versus denotes the final misfit-weighted averaged model.

Figure 7 shows an example of a DAS-based surface wave inversion utilizing the multimode dispersion curve picks from Figure 6b. For all modes, acceptable misfits between the observed and inverted dispersion curves are obtained (Figure 7a1–7a4). In order to verify the accuracy of the inverted velocity model, we generate a synthetic shot gather using a finite-difference solver, SOFI2D (Bohlen, 2002), to allow direct comparison of various wave modes. A horizontal force with source signature defined by the EGF autocorrelation function at location ~22 km is used as the source input function. We use a grid spacing of 20 m in both X and Z to avoid numerical dispersion; a time step of 0.5 millisecond is used to guarantee model stability. Figure 8 shows a direct comparison of the modeled shot gather (blue) and the measured Rayleigh waves using DAS (red). The modeled and observed waveforms are highly consistent in terms of kinematics and bolster our confidence in the accuracy of the

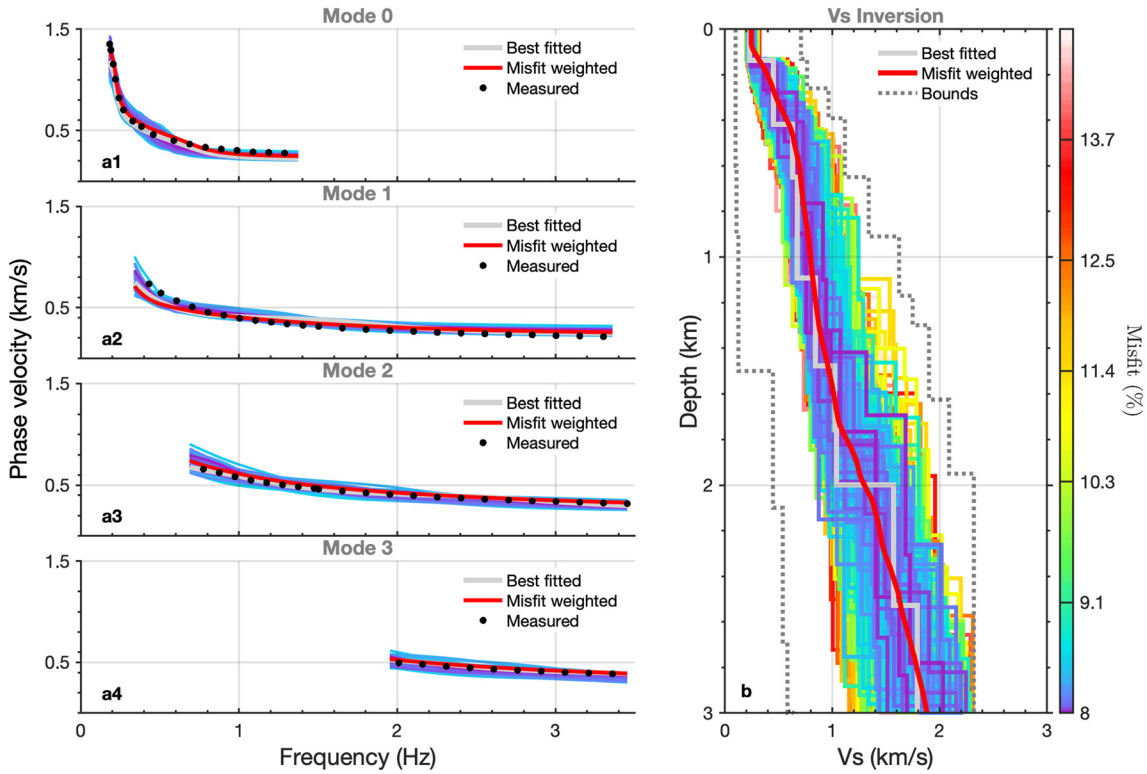

Figure 7. Distributed acoustic sensing-based multimode surface wave dispersion inversion. Panel (a) shows the measured (the black dotted curves) and the best 400 forward (the colored curves) dispersion curves; the gray curves show the dispersion curve from the best-fitting model; the red curves depict the dispersion curve modeled from the misfit-weighted mean model. Panel (b) presents the best 400 V_s models; the gray and red curves indicate the best fitted model and the misfit-weighted median model; the gray dashed lines indicate the upper and bottom velocity boundaries. Colors in (a and b) are coded by misfits as shown on the color map.

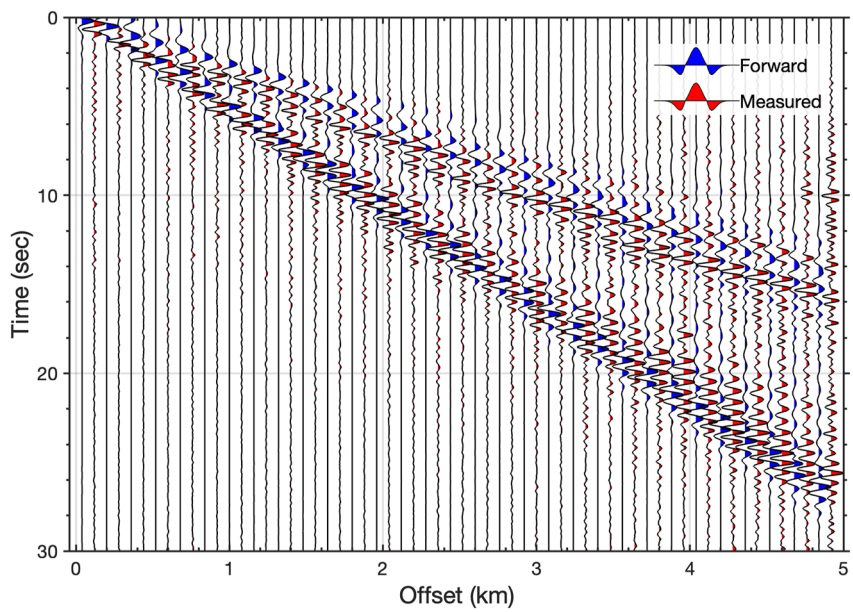

Figure 8. Comparison between the forward waveforms, based on the inverted Versus model in this figure, and the observed Rayleigh waves recovered from distributed acoustic sensing ambient noise interferometry in Figure 7. A bandpass filter between 0.1 and 5 Hz is applied to the combined waveforms. The blue color filled traces represent the forward waveforms; the red color filled traces represent the measured waveforms. Clear consistency can be observed between two types of waveforms. Note that, the forward modeled waveforms are exported as the default unit of particle velocity instead of strain rate, so we did not apply trace-by-trace waveform fitting comparison here.

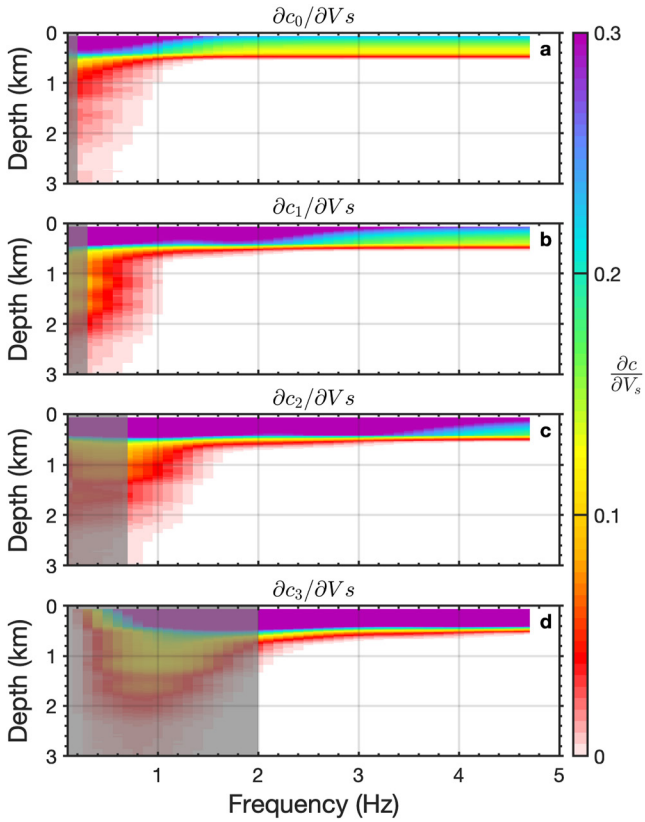

Figure 9. Sensitivity kernel of the fundamental (a), first higher mode (b), second higher mode (c) and third higher mode (d) surface waves, respectively. c_i ($i = 0 \ldots 3$) denotes the phase velocity at fundamental and higher modes; V_s denotes the Shear wave velocity. The gray zone indicates the frequency band that could not be reliably identified in the distributed acoustic sensing dispersion analysis.

recovered velocity model. Some local differences, particularly in amplitudes and frequency components at far offset, are also visible; this is likely due to a combination of source wavelet accuracy and the absence of attenuation (Q) in the forward model.

We used the Computer Programs in Seismology (CPS) package (Herrmann, 2013) to compute dispersion curves and Fréchet sensitivity kernels for further analysis. The forward modeled dispersion curves from the misfit-weighted model (the red curve in Figure 7b) also show a good match with the measured picks. Figure 9 shows the sensitivity kernels of different Rayleigh wave modes; compared with the sensitivity kernel of the fundamental mode (Figure 9a), higher sensitivities are observed at deeper depths for the lower frequency band of the first overtone (Figure 9b) and at shallower depth for higher frequencies of all the higher modes (Figures 9b–9d). These observations indicate that simultaneous inversion of multiple modes has advantages over using only the fundamental mode, both reducing non-uniqueness and improving sensitivity at depth (Beaty et al., 2002; Fu et al., 2022; L. Pan et al., 2019; Xia et al., 2012).

4. Results

Our high-resolution inverted V_s model, based on the initial model (Figure 10a) derived from the picked dispersion curves along our DAS array, is shown in Figure 10c with the Unified Community Velocity Model (UCVM) (Small et al., 2017) shown for comparison (Figure 10b). The unified community velocity model in the Imperial Valley is constrained by a combination of regional earthquake picks and active source travel-time data collected by the Salton Sea Seismic Imaging Project, SSIP (Ajala et al., 2019; Persaud et al., 2016). While both models are broadly similar in depth, our inversion resolves a zone of high S-wave velocity beneath the BGF which is only hinted at in the unified community velocity model. Likewise, the DAS V_s profile resolves two zones of lower S-wave velocity north and south of the BGF. The high velocity zone is also coincident with a region of elevated V_p at 3 km depth (see the reference V_p model on Figure S3 in Supporting Information S1) observed in SSIP inversions (Han et al., 2016; Persaud et al., 2016). To evaluate the sensitivity of the observed high S-wave velocity zone to the choice of initial earth model, we conducted an identical inversion using the interpolated unified community velocity model as a starting model. The results are quite similar in terms of both the location and magnitude of the anomaly (see Figure S4 in Supporting Information S1).

At the 5 km location, where our DAS cable crosses over the Alamo River, a low-velocity zone (LVZ) is visible on the inverted V_s structure as indicated by the magenta arrow on Figure 10b, and coincides with the LVZ hinted at by the unified community velocity model as indicated by the dip in the 1.5 km/s contour line around the 5 km location on Figure 10a. This LVZ could indicate an unmapped fault located between Calipatria and Brawley; a localized discontinuity has also been inferred from electrical log offsets (Towse & Palmer, 1976), surface magnetic surveys (Meidav & Furgerson, 1972), and a seismic refraction survey conducted by Frith (1978). Around the 20 km location, a second LVZ indicated by the break contour line at 1.8 km/s on the DAS result could be associated with the previously mapped Brawley Fault (BF) and the complex fault network associated with the southern termination of the Brawley Seismic Zone. The mapped Brawley Fault from USGS Quaternary fault database crosses our cable at ~21 km location on the surface (see Figure 1a), and our model indicates that it might extend farther to the north at depth.

Discontinuities in EGF waveform character (Figure 10d), observed on common offset (5 km) gathers derived from interferometric processing, also support these observations and suggest a substantial structural contrast across the previously mentioned transition regions. The earlier/faster wave train around the BGF area, likely Rayleigh wave components and highlighted by the red dashed curve, indicates the higher velocity structure which is consistent with the observations on the inverted V_s model (Figure 10c). We hypothesize that this feature is

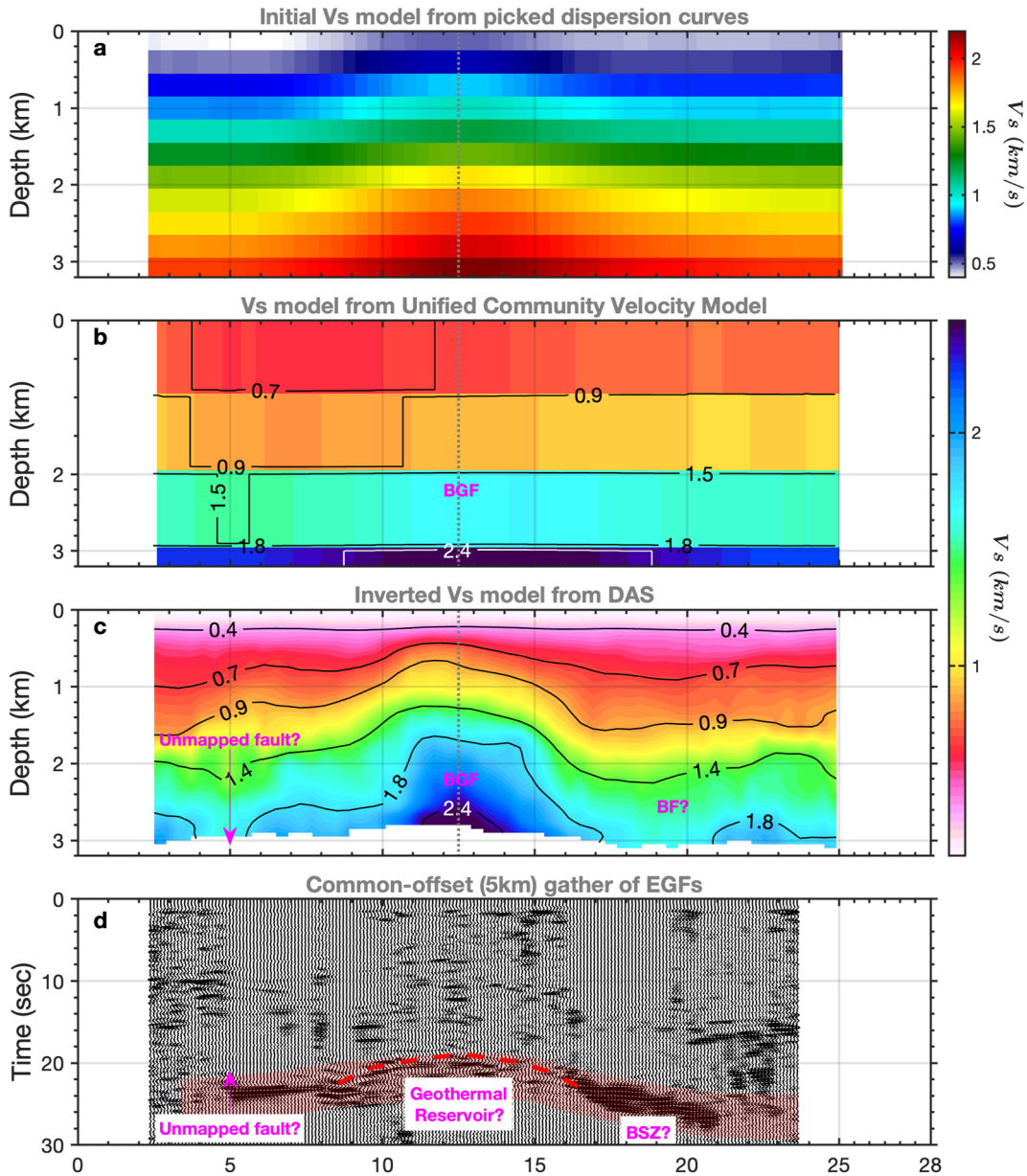

Figure 10. V_s imaging of the Brawley geothermal reservoir and Brawley fault. (a) Initial V_s model converted from picked dispersion curves based on Equation 2. (b) Reference V_s model from the unified community velocity model. (c) Inverted V_s model from distributed acoustic sensing ambient noise data. The gray dashed line indicates the location of the model used for comparison in Figure 12a. The black lines show the contour lines for V_s. (d) Common-offset gather derived from the retrieved EGFs with interval distance of 5 km. The red shadow zone highlights the discontinuities in the fundamental EGF waveform character.

due to secondary mineral precipitation caused by hydrothermal brine circulation and corresponding water-rock interaction at depth. Discontinuities of the waveforms at two sides of the 5 km location, including both the fundamental EGFs highlighted by the red shadow zone and higher overtones arrived around 10 s, suggest an unmapped structural feature, possibly fault-related. The complex waveforms around 20 km may be related to the complex fault convergence at the termination of the Brawley Seismic Zone.

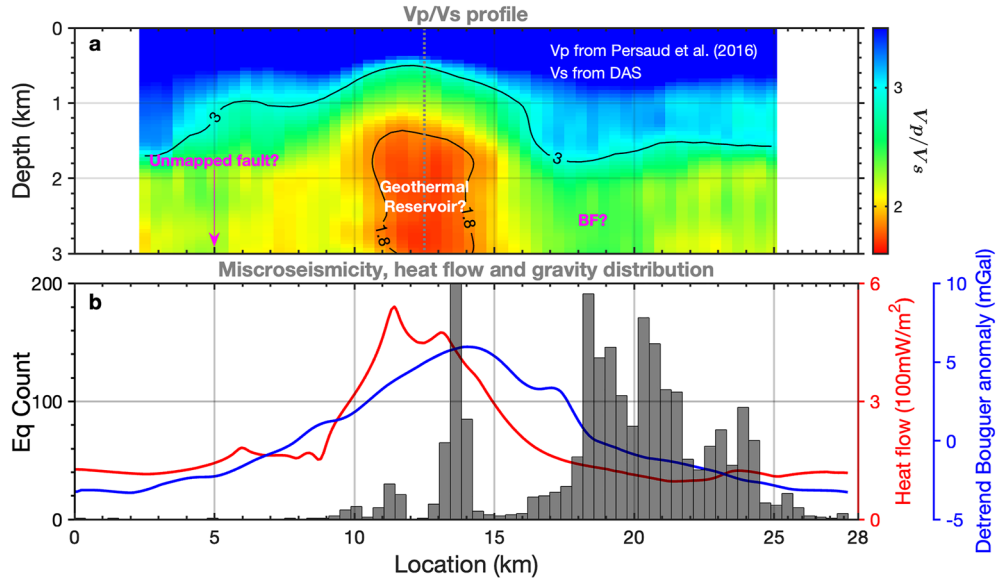

Figure 11. Seismic imaging of Brawley geothermal reservoir and Brawley fault. (a) V_p/V_s profile based on V_p from Persaud et al. (2016) and V_s from distributed acoustic sensing. The gray dashed line indicates the location of the model used for comparison in Figure 12a. (b) Distribution of microseismicity, heat flow, and the detrended Bouguer gravity anomaly along the ~28 km fiber-optic cable. For better visualization, the linear trend of the Bouguer gravity has been removed.

5. Discussion

5.1. Geothermal Imaging Using V_p/V_s

In geothermal settings within sedimentary basins, high seismic velocities are often associated with low porosity units with high degrees of cementation and/or secondary alteration (e.g., McGuire et al., 2015; Ryan & Shalev, 2014). Constraints on the ratio of P- to S-wave velocities (V_p/V_s) can help to clarify the nature of subsurface anomalies and is sometimes a more significant indicator than V_p or V_s separately in identifying the presence of fractures and the effects of pore pressure (Behm et al., 2019; Hamada, 2004; Nakajima et al., 2001; Takei, 2002; Walck, 1988). We utilize the V_p model from SSIP by slicing the three-dimensional (3D) model of Persaud et al. (2016) along our DAS cable and interpolating the 2D slice to the same grid as our inverted V_s model (see the reference V_p model on Figure S3 in Supporting Information S1). Compared with the inverted 2D V_s model, the reference 2D V_p model exhibits lower spatial resolution due to the limited shot and receiver coverage in the SSIP experiment. Although the obtained V_p/V_s model does not have as high a spatial resolution as the original V_s model, it is still a useful aid in interpreting the lateral variations beneath the BGF. A similar V_p/V_s profile can also be obtained by using the original reference V_p model and a version of the DAS V_s model downsampled to the same resolution (Figure S5 in Supporting Information S1).

The resulting mapped V_p/V_s profile (Figure 11a) displays a prominent low V_p/V_s feature near the BGF area, as indicated by the contour line at $V_p/V_s = 1.8$. It coincides with observations presented in Lin (2013), which show that one of the most significant features in the V_p/V_s model for the Salton Trough is a zone of low V_p/V_s values below 2 km depth, and the lowest V_p/V_s ratios occur in the SSGF area with values varying from 1.510 to 1.811 according to Lin (2020). In addition to the low V_p/V_s feature, likely associated with the BGF geothermal reservoir or underlying structures, two high V_p/V_s zones around 5 and 20 km locations are co-located with low velocity zones observed on the inverted V_s profile. This observation agrees with our hypothesis that these features are damage zones related to faulting.

This low V_p/V_s feature is strikingly correlated with a high heat flow anomaly (the red curve in Figure 11b) as well as a gravity high (the blue curve in Figure 11b). The higher Bouguer gravity anomaly near the heat flow anomaly (Figure 1b) may result from intrusion of basaltic dikes or the reduction of sediment porosity due to hydrothermal brine circulation (Mase et al., 1981).

Boreholes in geothermal areas in the Imperial Valley have encountered greenschist facies metamorphism, reduced porosity due to cement in-fill, altered rhyolites, and basalt dikes. Several prior geologic studies have concluded

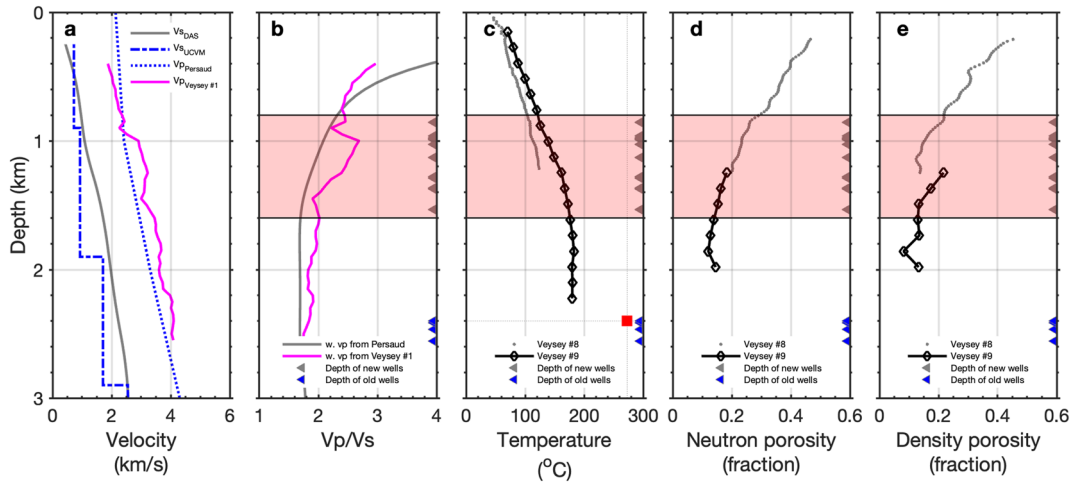

Figure 12. Velocity models, borehole observations and the inferred geothermal system. (a) Velocity models at location 12.5 km (highlighted by the gray dashed line in Figures 10 and 11). V_s model from distributed acoustic sensing (DAS) (the gray solid line) and the unified community velocity model (the blue dotted-dashed line), V_p model from Persaud et al. (2016) (the blue dotted line) and geothermal well Veysey #1 (the magenta solid line). (b) V_p/V_s profile at location 12.5 km with V_s from DAS and V_p from Persaud et al. (2016) (the gray dotted line) and geothermal well Veysey #1 (the magenta solid line). Panels (c–e) show the smoothed temperature, neutron and density porosity observations from geothermal wells, Veysey #8 (the gray dotted line) and Veysey #9 (the black diamond line), respectively. The gray triangles indicate the depths of the new production wells developed by Ormat Nevada Inc; the blue triangles indicate the depths of the older production wells developed by Unocal. The red square in c shows the temperature record observed in old geothermal well of Unocal.

that hydrothermal alteration can have a pronounced effect on the physical properties of the sediments by reducing porosity and increasing density (Browne, 1976; Elders et al., 1979; McDowell, 1987; McDowell & Elders, 1979; Miller & Elders, 1980; Muffler & White, 1969; Robinson et al., 1976). These hydrothermal alteration effects may coincide with the observation of low V_p/V_s anomalies on Figure 11a, which might be used as an indicator for the "roots" of high-temperature geothermal systems.

The Imperial Valley exhibits active deformation and seismicity associated with both extension within the rift centers and shear across strike-slip faults systems (Elders et al., 1972; Han et al., 2016; Parsons & McCarthy, 1996). The relocated historical earthquakes (Figure 1a) from 1981 to 2019 (Hauksson et al., 2012), with most of seismic events occurring in the Brawley Seismic Zone, indicate the northernmost extension of the spreading center axis associated with the East Pacific Rise. In order to statistically analyze the distribution of seismicity along our DAS cable, we project the near-line (distance <2 km) events to the vertical plane where our DAS cable is located. Abundant earthquakes are distributed around the 20 km location (as shown on the histogram on Figure 11b); this observation is consistent with interpreting the high V_p/V_s values as damage related to faulting at the terminus of the Brawley Seismic Zone (Choi et al., 2016). However, the relationship between the seismicity and the V_p/V_s distribution is still ambiguous considering the substantial offset between our inversion depth (<3 km) and the relocated earthquake depths ranging mainly between 5 and 10 km (Hauksson et al., 2012). Earthquakes occurring in the BGF area at depths from 10 to 15 km (much deeper than the geothermal reservoir) may have a remote connection to shallower hydrothermal systems or at least related structures (Ellsworth, 2013); the histogram peak around 13.5 km is associated with the 2012 Brawley swarm (Wei et al., 2013), which has been hypothesized to be induced indirectly through poroelastic coupling rather than directly through pore pressure change (Wei et al., 2015). During our DAS deployment, the primary seismic network observed no events close to the BGF despite varying production rates, suggesting that the current production/injection strategy employed at the field is not strongly coupled to local seismicity.

5.2. Brawley Geothermal Field System

The Brawley geothermal field was discovered and developed by Union Oil Company (Unocal) in the 1980's. Initial characterization and exploitation of the field involved drilling a sequence of deep (1.5–2.1 km) geothermal wells and operation of a 10 MWe power plant. The high dissolved solids content of this deep resource resulted

in corrosion and scaling issues for the plant and the facility was eventually closed. Ormat Nevada Inc subsequently investigated geothermal production from a shallower sandstone unit in 2006 and found that sufficient matrix permeability and porosity existed for production and operation of a binary-type plant. After resurrection of the previously developed geothermal field and the drilling and completion of new wells tapping the shallower (0.5–1.4 km) reservoir, a power plant with a nameplate capacity of 49.9 MWe is currently operating (Matlick & Jayne, 2008).

To better evaluate the geothermal system beneath the Brawley field, we focus on the depth variation of the low V_p/V_s anomalies detected by DAS as well as observations from three nearby geothermal wells (magenta triangles in Figure 1a). For better display, well logs are smoothed with a 150 m averaging window (Figure S6 in Supporting Information S1 provides images of the original well logs).

Figure 12a provides a comparison between various velocity models in BGF area, which allows assessment of the obtained structural models. Compared with the lower resolution V_s model from the unified community velocity model (the blue dotted-dashed line), the inverted V_s model obtained using DAS (the gray solid line) shows a similar trend; the reference V_p model (the blue dotted line) is smoother but generally matches the sonic log from the Veysey #1 geothermal well (the magenta line). We observe that the V_p/V_s model utilizing the reference V_p from Persaud et al. (2016) (the gray line in Figure 12b) matches well with the one with the reference V_p from the sonic log (the magenta line in Figure 12b), except for the shallower zones where the V_p model was poorly resolved from travel-time tomography in Persaud et al. (2016).

The updated V_p/V_s model, using the high-resolution V_p model from the sonic log, gradually decreases from a value of 3 to 2.2 until a depth of 800 m; then rapidly increases from 2.2 to 2.7 and decreases again to a relatively constant value of ∼1.8 at depths below 1,600 m. We interpret the small zone of increasing V_p/V_s to be associated with the higher porosity upper geothermal reservoir, dominated by small-scale fractures which can be reactivated, after being filled, with high fluid pressures in the reservoir (Younker et al., 1982). This interval is also closely aligned with the vertical depths and completions of the 18 new production wells highlighted by the gray triangles on Figures 12b–12d.

Hydrothermal alteration of reservoir rocks leads to the self-sealing process and can create impermeable cap rocks over geothermal reservoirs (Facca & Tonani, 1967). In our V_p/V_s model, however, any interface between the upper reservoir and altered zones above is ambiguous due to the lower resolution of the inverted V_s model in comparison to the sonic log-derived V_p model. The zone at lower depths with almost constant, low V_p/V_s houses the lower geothermal reservoir, likely dominated by larger fractures with potential cementation, recrystallization, and thermal metamorphism caused by circulating hydrothermal fluids. Seismic as well as "silent" slip, both significant at the Brawley field (Materna et al., 2022), may assist in maintaining fracture permeability in the deeper reservoir sections.

Historical logs show dramatically reduced temperature gradients with depth below 800 m, from approximately 85°C/km to 3°C/km and nearly constant at greater depths. The transition in the character of the gradient occurs within the upper geothermal reservoir (highlighted by the light-red shallow zone on Figure 12c), and it might indicate a change in the mode of heat transport. The constant temperature records from Veysey #9 well in the lower reservoir, with low gradients of ∼1°C/km, suggest that convection is occurring at depths below ∼1.6 kmin the Brawley system. However, we do not have information on the timing of the historical temperature logs with respect to well drilling, completion, and other in-well operations so a risk exists that these lower gradients might be influenced by near-well thermal transients. The fact that a hotter reported point measurement was made in the Veysey #9 well suggests that the available logs may not fully capture the temperature profile. Reduced porosity is observed in the lower reservoir compared to that in the upper reservoir (Figures 12d and 12e), consistent with both seismic observations and the Bouguer anomaly. We hypothesize that this is due to hydrothermal alteration of this section of the reservoir.

As mentioned previously, the lower reservoir is where Unocal identified the fractured high-temperature resource with fluid temperatures of up to 273°C (the red square on Figure 12c) and operated the older production wells (the blue triangles on Figures 12b–12d). Unfortunately, high salinity brine and the non-condensable gas caused the carbon steel casing and surface equipment to rapidly develop scale and corrode; this problem led Unocal to abandon the project since the early exploration focus was on the higher temperature resources.

Our high-resolution 2D V_s profile from DAS ambient noise successfully mapped the thermally altered zone of the high-temperature geothermal reservoir. We should note that the low V_p/V_s region is likely a signature of the lower matrix porosity and altered mineral assemblages, driven by localized heat flow, rather than related to fracture

permeability which would have the opposite trend. In this sense, the high V_s values and low V_p/V_s ratio are acting as a seismic "geothermometer" (Ryan & Shalev, 2014) for alteration zones. If validated, this might provide a strategy for seismically identifying local hot spots for further exploratory studies. Further work investigating the seismic rock physics of the Brawley field, similar to studies conducted near the Salton Sea (Bonner et al., 2006), would aid more quantitative interpretation of similar regional data.

With the assistance of legacy sonic logs, the improved 1D V_p/V_s model with higher vertical resolution also detected the weakly thermally altered upper geothermal reservoir, which contains moderately saline water and relatively high porosity. Unfortunately, it is challenging to distinguish this upper reservoir with ambient noise results alone due to the limited vertical resolution of the seismic imaging technique. While we would also expect a somewhat higher V_p/V_s ratio in the flowing zones of the lower reservoir due to fracturing, our surface wave study likely has insufficient resolving power to isolate such localized features at depth. Further work is required to image fine-scale crustal structures beneath linear arrays, using for example, waveform-based inversion methods (Y. Pan et al., 2021; Zhang et al., 2018) or extraction of refracted body waves and/or reflected phases from the ambient noise wavefield.

6. Conclusions

We extract high-quality surface waves from ambient noise data acquired using distributed acoustic sensing (DAS) and a 28-km-long telecommunication cable, and apply high-resolution surface wave imaging to retrieve the S wave velocity structure of the top 3 km of the Imperial Valley. We develop a linear spatial stacking technique, referred to as bin stacking, to attenuate spurious events associated with persistent localized sources and enhance the quality of the retrieved empirical Green's function (EGF). We jointly invert multiple surface wave modes retrieved from this data set to reduce non-uniqueness inherent in V_s inversion and improve sensitivity at depth. Based on our inverted V_s model and the V_p model obtained from Persaud et al. (2016), we generate a 2D V_p/V_s profile across the valley, and observe a significant low V_p/V_s feature beneath the Brawley field, which is likely related to hydrothermal alteration within and beneath the currently producing reservoir. We have also identified two low velocity zones, north and south of the field, which we hypothesize are associated with an unmapped fault between Calipatria and Brawley and the mapped Brawley Fault and Brawley Seismic Zone termination zone, respectively, although this association is slightly more speculative.

With the assistance of legacy sonic logs, we were also able to improve the 1D V_p/V_s model, allowing potential identification of the seismic signature associated with the upper geothermal reservoir. Based on observations from wireline data, heat flow, and gravity surveys, we attempt to understand the geophysical signatures of different geothermal system components including the upper and lower reservoir units at the field. Nevertheless, further investigation would be required to validate components of our interpretation, particularly refinement of our V_p model to better relate our DAS observations ambient noise observations to the rock properties. While future studies might benefit from incorporation of a larger variety of wave modes and earthquake signals recorded on the same network, our investigation effectively demonstrates the utility of high spatial-resolution geothermal characterization with DAS at the basin scale, as well as the potential for high temporal-resolution geothermal monitoring even with the short imaging period (2 days).

Appendix A: Imperial Valley Dark Fiber Team

The Imperial Valley Dark Fiber Team includes Jonathan Ajo-Franklin (Rice University), Feng Cheng (Zhejiang University and Rice University), Verónica Rodríguez Tribaldos (GFZ Potsdam and LBNL), Avinash Nayak (LBNL), Todd Wood (LBNL), Michelle Robertson (LBNL), Kesheng Wu (LBNL), Bin Dong (LBNL), Patrick Dobson (LBNL), Robert Mellors (Scripps Institution of Oceanography), Cody Rotermund (ESnet and LBNL), Benxin Chi (Chinese Academy of Sciences, formerly Rice University); Eric Matzel (LLNL), Dennise C. Templeton (LLNL), Christina Morency (LLNL).

Data Availability Statement

The extracted empirical Green's functions, the picked dispersion curves, and the inverted shear velocity model used in this work, as well as 40 min of raw DAS waveforms, are available in the following OSF repository: https://osf.io/ckt9q. The three geothermal wells used in Figure 11 are digitized from https://www.conservation.ca.gov/

with API #02590043/02590182/02590183. The Geopsy package 3.3.6 is available at https://www.geopsy.org/download.php. The SOFI2D package is available at https://git.scc.kit.edu/GPIAG-Software/SOFI2D. The CPS package 3.30 is available at https://www.eas.slu.edu/eqc/eqccps.html. The phase-weight slant-stacking algorithm can be found at https://github.com/marscfeng/pwslantstacking. All websites were last accessed in Dec 2022.

Acknowledgments
The Imperial Valley Dark Fiber Project was supported by the Office of Energy Efficiency and Renewable Energy (EERE), Geothermal Technologies Office (GTO), U.S. Department of Energy (DOE) under Award Number DE-AC02-05CH11231 with Lawrence Berkeley National Laboratory (LBNL). We would like to thank Thomas Coleman and Silixa LLC for useful acquisition suggestions and Zayo for fiber access and field support at the Calipatria ILA. We are very grateful to Karina Mellors and Dave Sandwell for assistance with tap tests. We thanks Jacob DeAngelo of the USGS for providing heat flow data and Shengji Wei of the Nanyang Technological University for providing the location information of geothermal wells in BGF. We would also like to thank Prof. Shawn Biehler (UCR) for providing a subset of his gravity database relevant to our study and Naod Arya for assisting with obtaining and managing our wireline log collection. The 1981–2019 earthquake catalog for Southern California is downloaded from Southern California Earthquake Data Center (SCEDC, last access February 2022). The SCEDC and Southern California Seismic Network (SCSN) are funded through U.S. Geological Survey Grant G20AP00037, and the Southern California Earthquake Center, which is funded by NSF Cooperative Agreement EAR-0529922 and USGS Cooperative Agreement 07HQAG0008. The Quaternary faults are obtained from the USGS Quaternary fault database (https://usgs.maps.arcgis.com/apps/webappviewer/index.html?id=5a6038b3a1684561a9b0aadf88412fcf). We would like to acknowledge the use of the SCEC Unified Community Velocity Model Software (Small et al., 2017) in this research. Lastly, we thank John Akerley of Ormat for sharing a subset of data related to the Brawley geothermal field. We sincerely thank Editor Douglas Schmitt and two anonymous reviewers for their time and valuable suggestions.

References

Ajala, R., Persaud, P., Stock, J. M., Fuis, G. S., Hole, J. A., Goldman, M., & Scheirer, D. (2019). Three-dimensional basin and fault structure from a detailed seismic velocity model of Coachella Valley, Southern California. *Journal of Geophysical Research: Solid Earth*, *124*(5), 4728–4750. https://doi.org/10.1029/2018jb016260

Ajo-Franklin, J., Dou, S., Lindsey, N., Monga, I., Tracy, C., Robertson, M., et al. (2019). Distributed acoustic sensing using dark fiber for near-surface characterization and broadband seismic event detection. *Scientific Reports*, *9*(1), 1328. https://doi.org/10.1038/s41598-018-36675-8

Ajo-Franklin, J., Rodríguez Tribaldos, V., Nayak, A., Cheng, F., Mellors, R., Chi, B., et al. (2022). The Imperial Valley Dark Fiber Project: Towards seismic studies using DAS and telecom infrastructure for geothermal applications. *Seismological Research Letters*, *93*(5), 2906–2919. https://doi.org/10.1785/0220220072

Anderson, E., Crosby, D., & Ussher, G. (2000). Bulls-eye! simple resistivity imaging to reliably locate the geothermal reservoir. In *Proceedings World Geothermal Congress* (pp. 909–914).

Ars, J.-M., Tarits, P., Hautot, S., Bellanger, M., Coutant, O., & Maia, M. (2019). Joint inversion of gravity and surface wave data constrained by magnetotelluric: Application to deep geothermal exploration of crustal fault zone in felsic basement. *Geothermics*, *80*, 56–68. https://doi.org/10.1016/j.geothermics.2019.02.006

Atef, H., Abd El-Gawad, A., Zaher, M. A., & Farag, K. (2016). The contribution of gravity method in geothermal exploration of southern part of the Gulf of Suez-Sinai region, Egypt. *NRIAG Journal of Astronomy and Geophysics*, *5*(1), 173–185. https://doi.org/10.1016/j.nrjag.2016.02.005

Beaty, K. S., Schmitt, D. R., & Sacchi, M. (2002). Simulated annealing inversion of multimode Raleigh wave dispersion curves for geological structure. *Geophysical Journal International*, *151*(2), 622–631. https://doi.org/10.1046/j.1365-246x.2002.01809.x

Behm, M., Cheng, F., Patterson, A., & Soreghan, G. (2019). Passive processing of active nodal seismic data: Estimation of V_p/V_s ratios to characterize structure and hydrology of an alpine valley infill. *Solid Earth*, 1–32. https://doi.org/10.5194/se-2019-47

Bensen, G., Ritzwoller, M., Barmin, M., Levshin, A., Lin, F., Moschetti, M., et al. (2007). Processing seismic ambient noise data to obtain reliable broad-band surface wave dispersion measurements. *Geophysical Journal International*, *169*(3), 1239–1260. https://doi.org/10.1111/j.1365-246x.2007.03374.x

Biehler, S. (1964). *A geophysical study of the Salton Trough of southern California* (Unpublished doctoral dissertation). California Institute of Technology.

Biehler, S. (1971). *Gravity studies in the Imperial Valley*. *Cooperative geological-geophysical-geochemical investigations of geothermal resources in the Imperial Valley of California: Riverside, California* (pp. 29–41). University of California–Riverside Education Research Service.

Bohlen, T. (2002). Parallel 3-D viscoelastic finite difference seismic modelling. *Computers & Geosciences*, *28*(8), 887–899. https://doi.org/10.1016/s0098-3004(02)00006-7

Bonner, B., Hutchings, L., & Kasameyer, P. (2006). *A strategy for interpretation of microearthquake tomography results in the Salton Sea Geothermal Field based upon rock physics interpretations of state 2-14 borehole logs* (Technical Report). Lawrence Livermore National Lab.

Booth, A. D., Christoffersen, P., Schoonman, C., Clarke, A., Hubbard, B., Law, R., et al. (2020). Distributed acoustic sensing of seismic properties in a borehole drilled on a fast-flowing Greenlandic outlet glacier. *Geophysical Research Letters*, *47*(13), e2020GL088148. https://doi.org/10.1029/2020gl088148

Brodsky, E. E., & Lajoie, L. J. (2013). Anthropogenic seismicity rates and operational parameters at the Salton Sea Geothermal Field. *Science*, *341*(6145), 543–546. https://doi.org/10.1126/science.1239213

Brogi, A., Lazzarotto, A., Liotta, D., Ranalli, G., & CROP18 Working Group. (2005). Crustal structures in the geothermal areas of southern Tuscany (Italy): Insights from the CROP 18 deep seismic reflection lines. *Journal of Volcanology and Geothermal Research*, *148*(1–2), 60–80. https://doi.org/10.1016/j.jvolgeores.2005.03.014

Browne, P. (1976). *Occurrence of hydrothermal alteration of diabase Heber geothermal field, Imperial Valley, California. Preliminary results* (Technical Report). University of California Riverside, Institute of Geophysics Planetary Physics Report.

Burton-Johnson, A., Dziadek, R., & Martin, C. (2020). Geothermal heat flow in Antarctica: Current and future directions. *The Cryosphere*, *14*(11), 3843–3873. https://doi.org/10.5194/tc-14-3843-2020

Campillo, M., & Paul, A. (2003). Long-range correlations in the diffuse seismic coda. *Science*, *299*(5606), 547–549. https://doi.org/10.1126/science.1078551

Cedilnik, G., Lees, G., Schmidt, P., Herstrøm, S., & Geisler, T. (2019). Ultra-long reach fiber distributed acoustic sensing for power cable monitoring. In *Proceedings of the JICABLE* (Vol. 19).

Chalari, A., Mondanos, M., Coleman, T., Farhadiroushan, M., & Stork, A. (2019). Seismic methods for geothermal reservoir characterization and monitoring using fiber optic distributed acoustic and temperature sensor. In *EAGE/BVG/FKPE Joint Workshop on Borehole Geophysics and Geothermal Energy* (Vol. 2019, pp. 1–6).

Chang, H., & Nakata, N. (2022). Investigation of time-lapse changes with DAS borehole data at the brady geothermal field using deconvolution interferometry. *Remote Sensing*, *14*(1), 185. https://doi.org/10.3390/rs14010185

Cheng, F., Chi, B., Lindsey, N., Dawe, C., & Ajo-Franklin, J. (2021). Utilizing distributed acoustic sensing and ocean bottom fiber optic cables for submarine structural characterization. *Scientific Reports*, *11*(1), 5613. https://doi.org/10.1038/s41598-021-84845-y

Cheng, F., Correa, J., Dou, S., Freifeld, B., Wood, T., Nihei, K., et al. (2021). Testing of a permanent orbital surface source and distributed acoustic sensing for monitoring of unconventional reservoirs: Preliminary results from the Eagle Ford Shale. *Geophysics*, *86*(2), P1–P12. https://doi.org/10.1190/geo2020-0403.1

Cheng, F., Lindsey, N. J., Sobolevskaia, V., Dou, S., Freifeld, B., Wood, T., et al. (2022). Watching the cryosphere thaw: Seismic monitoring of permafrost degradation using distributed acoustic sensing during a controlled heating experiment. *Geophysical Research Letters*, *49*(10), e2021GL097195. https://doi.org/10.1029/2021gl097195

Cheng, F., Xia, J., Ajo-Franklin, J. B., Behm, M., Zhou, C., Dai, T., et al. (2021). High-resolution ambient noise imaging of geothermal reservoir using 3C dense seismic nodal array and ultra-short observation. *Journal of Geophysical Research: Solid Earth*, *126*(8), e2021JB021827. https://doi.org/10.1029/2021jb021827

Cheng, F., Xia, J., Behm, M., Hu, Y., & Pang, J. (2019). Automated data selection in the Tau–*p* domain: Application to passive surface wave imaging. *Surveys in Geophysics*, *40*(5), 1–18. https://doi.org/10.1007/s10712-019-09530-2

Cheng, F., Xia, J., Luo, Y., Xu, Z., Wang, L., Shen, C., et al. (2016). Multi-channel analysis of passive surface waves based on cross-correlations. *Geophysics*, *81*(5), EN57–EN66. https://doi.org/10.1190/geo2015-0505.1

Cheng, F., Xia, J., Xu, Y., Xu, Z., & Pan, Y. (2015). A new passive seismic method based on seismic interferometry and multichannel analysis of surface waves. *Journal of Applied Geophysics*, *117*, 126–135. https://doi.org/10.1016/j.jappgeo.2015.04.005

Cheng, F., Xia, J., Xu, Z., Hu, Y., & Mi, B. (2018). Frequency-wavenumber (FK)-based data selection in high-frequency passive surface wave survey. *Surveys in Geophysics*, *39*(4), 661–682. https://doi.org/10.1007/s10712-018-9473-3

Cheng, F., Xia, J., Zhang, K., Zhou, C., & Ajo-Franklin, J. B. (2021). Phase-weighted slant-stacking for surface wave dispersion measurement. *Geophysical Journal International*, *226*(1), 256–269. https://doi.org/10.1093/gji/ggab101

Choi, J.-H., Edwards, P., Ko, K., & Kim, Y.-S. (2016). Definition and classification of fault damage zones: A review and a new methodological approach. *Earth-Science Reviews*, *152*, 70–87. https://doi.org/10.1016/j.earscirev.2015.11.006

Combs, J. (1978). *Geothermal exploration techniques: A case study*. *Final report (Coso geothermal area)* (Technical Report). Texas University, Center for Energy Studies.

Combs, J., & Hadley, D. (1977). Microearthquake investigation of the Mesa geothermal anomaly, Imperial Valley, California. *Geophysics*, *42*(1), 17–33. https://doi.org/10.1190/1.1440709

Dales, P., Audet, P., & Olivier, G. (2017). Seismic interferometry using persistent noise sources for temporal subsurface monitoring. *Geophysical Research Letters*, *44*(21), 10–863. https://doi.org/10.1002/2017gl075342

Daley, T. M., Freifeld, B. M., Ajo-Franklin, J., Dou, S., Pevzner, R., Shulakova, V., et al. (2013). Field testing of fiber-optic distributed acoustic sensing (DAS) for subsurface seismic monitoring. *The Leading Edge*, *32*(6), 699–706. https://doi.org/10.1190/tle32060699.1

Dobson, P. F. (2016). A review of exploration methods for discovering hidden geothermal systems. *GRC Transactions*, *40*, 695–706.

Dou, S., Lindsey, N., Wagner, A., Daley, T., Freifeld, B., Robertson, M., et al. (2017). Distributed acoustic sensing for seismic monitoring of the near surface: A traffic-noise interferometry case study. *Scientific Reports*, *7*(1), 1–12. https://doi.org/10.1038/s41598-017-11986-4

EIA. (2021). *Monthly energy review, April 2021* (Technical Report). Energy Information Administration. Retrieved from https://www.eia.gov/totalenergy/data/monthly/pdf/mer.pdf

Elders, W., Hoagland, J., McDowell, S., & Cobo, J. (1979). Hydrothermal mineral zones in the geothermal reservoir of Cerro Prieto. *Geothermics*, *8*(3–4), 201–209. https://doi.org/10.1016/0375-6505(79)90042-7

Elders, W., Rex, R., Robinson, P., Biehler, S., & Meidav, T. (1972). Crustal spreading in Southern California: The Imperial Valley and the Gulf of California formed by the rifting apart of a continental plate. *Science*, *178*(4056), 15–24. https://doi.org/10.1126/science.178.4056.15

Ellsworth, W. L. (2013). Injection-induced earthquakes. *science*, *341*(6142), 1225942. https://doi.org/10.1126/science.1225942

Facca, G., & Tonani, F. (1967). The self-sealing geothermal field. *Bulletin Volcanologique*, *30*(1), 271–273. https://doi.org/10.1007/BF02597674

Fahnestock, M., Abdalati, W., Joughin, I., Brozena, J., & Gogineni, P. (2001). High geothermal heat flow, basal melt, and the origin of rapid ice flow in central Greenland. *Science*, *294*(5550), 2338–2342. https://doi.org/10.1126/science.1065370

Fang, G., Li, Y. E., Zhao, Y., & Martin, E. R. (2020). Urban near-surface seismic monitoring using distributed acoustic sensing. *Geophysical Research Letters*, *47*(6), e2019GL086115. https://doi.org/10.1029/2019gl086115

Feigl, K. L., & Parker, L. M. (2019). *Porotomo final technical report: Poroelastic tomography by adjoint inverse modeling of data from seismology, geodesy, and hydrology* (Technical Report). University of Wisconsin. https://doi.org/10.2172/1499141

Feigl, K. L., & Team, P. (2017). Overview and preliminary results from the PoroTomo project at Brady Hot Springs, Nevada: Poroelastic tomography by adjoint inverse modeling of data from seismology, geodesy, and hydrology. In *Paper presented 42nd Workshop on Geothermal Reservoir Engineering* (pp. 1–15).

Fichtner, A., Bowden, D., & Ermert, L. (2020). Optimal processing for seismic noise correlations. *Geophysical Journal International*, *223*(3), 1548–1564. https://doi.org/10.1093/gji/ggaa390

Flóvenz, Ó. G., & Saemundsson, K. (1993). Heat flow and geothermal processes in Iceland. *Tectonophysics*, *225*(1–2), 123–138. https://doi.org/10.1016/0040-1951(93)90253-g

Foti, S., Hollender, F., Garofalo, F., Albarello, D., Asten, M., Bard, P.-Y., et al. (2018). Guidelines for the good practice of surface wave analysis: A product of the InterPACIFIC project. *Bulletin of Earthquake Engineering*, *16*(6), 2367–2420. https://doi.org/10.1007/s10518-017-0206-7

Frith, R. B. (1978). *Seismic refraction investigation of the Salton Sea geothermal area, Imperial Valley, California* (Technical Report). California University. Retrieved from https://www.osti.gov/servlets/purl/5716342

Fu, L., Pan, L., Li, Z., Dong, S., Ma, Q., & Chen, X. (2022). Improved high-resolution 3D Vs Model of Long Beach, CA: Inversion of multimodal dispersion curves from ambient noise of a dense array. *Geophysical Research Letters*, *49*(4), e2021GL097619. https://doi.org/10.1029/2021GL097619

Fuis, G. S., Mooney, W. D., Healey, J. H., McMechan, G., & Lutter, W. (1982). Crustal structure of the Imperial Valley region. *U. S. Geological Survey Professional Paper*, *1254*, 25–49.

Gao, J., Zhang, H., Zhang, S., Chen, X., Cheng, Z., Jia, X., et al. (2018). Three-dimensional magnetotelluric imaging of the geothermal system beneath the Gonghe Basin, Northeast Tibetan Plateau. *Geothermics*, *76*, 15–25. https://doi.org/10.1016/j.geothermics.2018.06.009

Gouedard, P., Stehly, L., Brenguier, F., Campillo, M., De Verdière, Y. C., Larose, E., et al. (2008). Cross-correlation of random fields: Mathematical approach and applications. *Geophysical Prospecting*, *56*(3), 375–393. https://doi.org/10.1111/j.1365-2478.2007.00684.x

Groos, J., & Ritter, J. (2009). Time domain classification and quantification of seismic noise in an urban environment. *Geophysical Journal International*, *179*(2), 1213–1231. https://doi.org/10.1111/j.1365-246x.2009.04343.x

GTO. (2022). *Fiscal Years 2022–2026 Multi-Year Program Plan* (Technical Report). U.S. Department of Energy, Office of Geothermal Technologies. Retrieved from https://www.energy.gov/sites/default/files/2022-02/GTO%20Multi-Year%20Program%20Plan%20FY%202022-2026.pdf

Guglielmetti, L., & Moscariello, A. (2021). On the use of gravity data in delineating geologic features of interest for geothermal exploration in the Geneva Basin (Switzerland): Prospects and limitations. *Swiss Journal of Geosciences*, *114*(1), 1–20. https://doi.org/10.1186/s00015-021-00392-8

Hamada, G. (2004). Reservoir fluids identification using Vp/Vs ratio? *Oil & Gas Science and Technology*, *59*(6), 649–654. https://doi.org/10.2516/ogst:2004046

Han, L., Hole, J. A., Stock, J. M., Fuis, G. S., Williams, C. F., Delph, J. R., et al. (2016). Seismic imaging of the metamorphism of young sediment into new crystalline crust in the actively rifting Imperial Valley, California. *Geochemistry, Geophysics, Geosystems*, *17*(11), 4566–4584. https://doi.org/10.1002/2016gc006610

Hartog, A. H. (2017). *An introduction to distributed optical fibre sensors*. CRC Press.

Hauksson, E., Stock, J., Bilham, R., Boese, M., Chen, X., Fielding, E. J., et al. (2013). Report on the August 2012 Brawley earthquake swarm in Imperial Valley, Southern California. *Seismological Research Letters*, *84*(2), 177–189. https://doi.org/10.1785/0220120169

Hauksson, E., Yang, W., & Shearer, P. M. (2012). Waveform relocated earthquake catalog for southern California (1981 to June 2011). *Bulletin of the Seismological Society of America*, *102*(5), 2239–2244. https://doi.org/10.1785/0120120010

Herrmann, R. B. (2013). Computer programs in seismology: An evolving tool for instruction and research. *Seismological Research Letters*, *84*(6), 1081–1088. https://doi.org/10.1785/0220110096

Herzig, C. T., & Jacobs, D. C. (1994). Cenozoic volcanism and two-stage extension in the Salton trough, southern California and northern Baja California. *Geology*, *22*(11), 991–994. https://doi.org/10.1130/0091-7613(1994)022<0991:cvatse>2.3.co;2

Hill, D. P. (1977). A model for earthquake swarms. *Journal of Geophysical Research*, *82*(8), 1347–1352. https://doi.org/10.1029/jb082i008p01347

Hill, D. P., Mowinckel, P., & Peake, L. G. (1975). Earthquakes, active faults, and geothermal areas in the Imperial Valley, California. *Science*, *188*(4195), 1306–1308. https://doi.org/10.1126/science.188.4195.1306

Hulen, J., & Pulka, F. S. (2001). Newly-discovered, ancient extrusive rhyolite in the Salton Sea geothermal field, Imperial Valley, California. In *Proceedings of the twenty-sixth workshop on geothermal reservoir engineering*.

Jackson, D. D. (1981). *Seismic and geodetic studies of the Imperial Valley, California* (Technical Report). Lawrence Livermore National Laboratory; California University.

Jin, G., & Roy, B. (2017). Hydraulic-fracture geometry characterization using low-frequency DAS signal. *The Leading Edge*, *36*(12), 975–980. https://doi.org/10.1190/tle36120975.1

Johnson, C. E., & Hadley, D. M. (1976). Tectonic implications of the Brawley earthquake swarm, Imperial Valley, California, January 1975. *Bulletin of the Seismological Society of America*, *66*(4), 1133–1144.

Kasahara, J., Hasada, Y., Kuzume, H., Fujise, Y., Mikada, H., & Yamamoto, K. (2020). Seismic feasibility study to identify and characterize supercritical geothermal reservoirs using DTS, DAS, and surface seismic array. In *Proceedings World Geothermal Congress* (p. 1).

Kaspereit, D., Mann, M., Sanyal, S., Rickard, B., Osborn, W., & Hulen, J. (2016). Updated conceptual model and reserve estimate for the Salton Sea geothermal field, Imperial Valley, California. *Geothermal Resources Council - Transactions*, *40*, 57–66.

Kratt, C., Coolbaugh, M., Sladek, C., Zehner, R., Penfield, R., & Delwiche, B. (2008). A new gold pan for the west: Discovering blind geothermal systems with shallow temperature surveys. *Geothermal Resources Council Transactions*, *32*, 153–158.

Lachenbruch, A., & Sass, J. (1973). Thermo-mechanical aspects of the San Andreas fault system. In *Proceedings of the Conference on the Tectonic Problems of the San Andreas fault system* (Vol. 13, pp. 192–205).

Larson, R. L., Menard, H., & Smith, S. (1968). Gulf of California: A result of ocean-floor spreading and transform faulting. *Science*, *161*(3843), 781–784. https://doi.org/10.1126/science.161.3843.781

Lehujeur, M., Vergne, J., Schmittbuhl, J., Zigone, D., Le Chenadec, A., & Team, E. (2018). Reservoir imaging using ambient noise correlation from a dense seismic network. *Journal of Geophysical Research: Solid Earth*, *123*(8), 6671–6686. https://doi.org/10.1029/2018jb015440

Lellouch, A., Lindsey, N. J., Ellsworth, W. L., & Biondi, B. L. (2020). Comparison between distributed acoustic sensing and geophones: Downhole microseismic monitoring of the FORGE geothermal experiment. *Seismological Society of America*, *91*(6), 3256–3268. https://doi.org/10.1785/0220200149

Lellouch, A., Schultz, R., Lindsey, N. J., Biondi, B., & Ellsworth, W. L. (2021). Low-magnitude seismicity with a downhole distributed acoustic sensing array—Examples from the forge geothermal experiment. *Journal of Geophysical Research: Solid Earth*, *126*(1), e2020JB020462. https://doi.org/10.1029/2020jb020462

Lin, G. (2013). Three-dimensional seismic velocity structure and precise earthquake relocations in the Salton trough, southern California. *Bulletin of the Seismological Society of America*, *103*(5), 2694–2708. https://doi.org/10.1785/0120120286

Lin, G. (2020). Spatiotemporal variations of in situ Vp/Vs ratio within the Salton Sea Geothermal Field, southern California. *Geothermics*, *84*, 101740. https://doi.org/10.1016/j.geothermics.2019.101740

Lin, G., Shearer, P. M., & Hauksson, E. (2007). Applying a three-dimensional velocity model, waveform cross correlation, and cluster analysis to locate southern California seismicity from 1981 to 2005. *Journal of Geophysical Research*, *112*(B12), B12309. https://doi.org/10.1029/2007jb004986

Lindsey, N. J., Dawe, T. C., & Ajo-Franklin, J. B. (2019). Illuminating seafloor faults and ocean dynamics with dark fiber distributed acoustic sensing. *Science*, *366*(6469), 1103–1107. https://doi.org/10.1126/science.aay5881

Lindsey, N. J., & Martin, E. R. (2021). Fiber-optic seismology. *Annual Review of Earth and Planetary Sciences*, *49*(1), 309–336. https://doi.org/10.1146/annurev-earth-072420-065213

Lindsey, N. J., Martin, E. R., Dreger, D. S., Freifeld, B., Cole, S., James, S. R., et al. (2017). Fiber-optic network observations of earthquake wavefields. *Geophysical Research Letters*, *44*(23), 11–792. https://doi.org/10.1002/2017gl075722

Lindsey, N. J., Rademacher, H., & Ajo-Franklin, J. B. (2020). On the broadband instrument response of fiber-optic DAS arrays. *Journal of Geophysical Research: Solid Earth*, *125*(2), e2019JB018145. https://doi.org/10.1029/2019jb018145

Lobkis, O. I., & Weaver, R. L. (2001). On the emergence of the Green's function in the correlations of a diffuse field. *Journal of the Acoustical Society of America*, *110*(6), 3011–3017. https://doi.org/10.1121/1.1417528

Lohman, R., & McGuire, J. (2007). Earthquake swarms driven by aseismic creep in the Salton Trough, California. *Journal of Geophysical Research*, *112*(B4), B04405. https://doi.org/10.1029/2006jb004596

Lomnitz, C., Mooser, F., Allen, C. R., Brune, J. N., & Thatcher, W. (1970). Seismicity and tectonics of the northern Gulf of California region, Mexico. Preliminary results. *Geofísica Internacional*, *10*(2), 37–48. https://doi.org/10.22201/igeof.00167169p.1970.10.2.1165

Lüschen, E., Dussel, M., Thomas, R., & Schulz, R. (2011). 3D seismic survey for geothermal exploration at Unterhaching, Munich, Germany. *First Break*, *29*(1). https://doi.org/10.3997/1365-2397.2011002

Marone, C. J., Scholtz, C., & Bilham, R. (1991). On the mechanics of earthquake afterslip. *Journal of Geophysical Research*, *96*(B5), 8441–8452. https://doi.org/10.1029/91jb00275

Martin, E. R., Castillo, C. M., Cole, S., Sawasdee, P. S., Yuan, S., Clapp, R., et al. (2017). Seismic monitoring leveraging existing telecom infrastructure at the SDASA: Active, passive, and ambient-noise analysis. *The Leading Edge*, *36*(12), 1025–1031. https://doi.org/10.1190/tle36121025.1

Martin, E. R., Lindsey, N. J., Ajo-Franklin, J. B., & Biondi, B. L. (2021). Introduction to interferometry of fiber-optic strain measurements. In Y. Li, M. Karrenbach, & J. B. Ajo-Franklin (Eds.), *Geophysical Monograph Series* (1st ed., pp. 111–129). Wiley. https://doi.org/10.1002/9781119521808.ch9

Martins, J. E., Ruigrok, E., Draganov, D., Hooper, A., Hanssen, R., White, R., & Soosalu, H. (2019). Imaging Torfajökull's magmatic plumbing system with seismic interferometry and phase velocity surface wave tomography. *Journal of Geophysical Research: Solid Earth*, *124*(3), 2920–2940. https://doi.org/10.1029/2018jb016002

Martins, J. E., Weemstra, C., Ruigrok, E., Verdel, A., Jousset, P., & Hersir, G. (2020). 3D S-wave velocity imaging of Reykjanes Peninsula high-enthalpy geothermal fields with ambient-noise tomography. *Journal of Volcanology and Geothermal Research*, *391*, 106685. https://doi.org/10.1016/j.jvolgeores.2019.106685

Mase, C., Sass, J., Brook, C., & Munroe, R. J. (1981). *Shallow hydrothermal regime of the East Brawley and Glamis known geothermal resource areas, Salton Trough, California* (Technical Report). Geological Survey.

Masoudi, A., & Newson, T. P. (2016). Contributed review: Distributed optical fibre dynamic strain sensing. *Review of Scientific Instruments*, *87*(1), 011501. https://doi.org/10.1063/1.4939482

Materna, K., Barbour, A., Jiang, J., & Eneva, M. (2022). Detection of aseismic slip and poroelastic reservoir deformation at the North Brawley Geothermal Field from 2009–2019. *Journal of Geophysical Research: Solid Earth*, *127*(5), e2021JB023335. https://doi.org/10.1029/2021JB023335

Matlick, S., & Jayne, T. (2008). Brawley—Resurrection of a previously developed geothermal field. *GRC Transactions*, *32*, 159–162.

McDowell, S. (1987). *Geothermal alteration of sediments in the Salton Sea scientific drill hole: Petrophysical properties and mass changes during alteration: Final report* (Technical Report). Michigan Technological University; Department of Geology and Geological Engineering. https://doi.org/10.2172/5434885

McDowell, S., & Elders, W. (1979). Geothermal metamorphism of sandstone in the Salton Sea geothermal system. *Guidebook: Geology and Geothermics of the Salton Trough* (pp. 70–76).

McGuire, J. J., Lohman, R. B., Catchings, R. D., Rymer, M. J., & Goldman, M. R. (2015). Relationships among seismic velocity, metamorphism, and seismic and aseismic fault slip in the Salton Sea Geothermal Field region. *Journal of Geophysical Research: Solid Earth*, *120*(4), 2600–2615. https://doi.org/10.1002/2014jb011579

Meidav, T., & Furgerson, R. (1972). Resistivity studies of the Imperial Valley geothermal area, California. *Geothermics*, *1*(2), 47–62. https://doi.org/10.1016/0375-6505(72)90012-0

Mi, B., Xia, J., Shen, C., Wang, L., Hu, Y., & Cheng, F. (2017). Horizontal resolution of multichannel analysis of surface waves. *Geophysics*, *82*(3), EN51–EN66. https://doi.org/10.1190/geo2016-0202.1

Miller, K. R., & Elders, W. A. (1980). *Geology, hydrothermal petrology, stable isotope geochemistry, and fluid inclusion geothermometry of LASL geothermal test well C/T-1 (Mesa 31-1), East Mesa, Imperial Valley, California, USA* (Technical Report). California University; Institute of Geophysics and Planetary Physics.

Muffler, L. P., & White, D. E. (1969). Active metamorphism of upper Cenozoic sediments in the Salton Sea geothermal field and the Salton Trough, southeastern California. *Geological Society of America Bulletin*, *80*(2), 157–181. https://doi.org/10.1130/0016-7606(1969)80[157:amoucs]2.0.co;2

Munoz, G. (2014). Exploring for geothermal resources with electromagnetic methods. *Surveys in Geophysics*, *35*(1), 101–122. https://doi.org/10.1007/s10712-013-9236-0

Nakajima, J., Matsuzawa, T., Hasegawa, A., & Zhao, D. (2001). Three-dimensional structure of Vp, Vs, and Vp/Vs beneath northeastern Japan: Implications for arc magmatism and fluids. *Journal of Geophysical Research*, *106*(B10), 21843–21857. https://doi.org/10.1029/2000jb000008

Nakata, N., Chang, J. P., Lawrence, J. F., & Boué, P. (2015). Body wave extraction and tomography at Long Beach, California, with ambient-noise interferometry. *Journal of Geophysical Research: Solid Earth*, *120*(2), 1159–1173. https://doi.org/10.1002/2015JB011870

Nakata, N., Snieder, R., Tsuji, T., Larner, K., & Matsuoka, T. (2011). Shear wave imaging from traffic noise using seismic interferometry by cross-coherence. *Geophysics*, *76*(6), SA97–SA106. https://doi.org/10.1190/geo2010-0188.1

Nayak, A., & Ajo-Franklin, J. (2021). Measurement of surface-wave phase-velocity dispersion on mixed inertial seismometer–distributed acoustic sensing seismic noise cross-correlations. *Bulletin of the Seismological Society of America*, *111*(6), 3432–3450. https://doi.org/10.1785/0120210028

Paitz, P., Edme, P., Gräff, D., Walter, F., Doetsch, J., Chalari, A., et al. (2021). Empirical investigations of the instrument response for distributed acoustic sensing (DAS) across 17 octaves. *Bulletin of the Seismological Society of America*, *111*(1), 1–10. https://doi.org/10.1785/0120200185

Paitz, P., Sager, K., & Fichtner, A. (2019). Rotation and strain ambient noise interferometry. *Geophysical Journal International*, *216*(3), 1938–1952. https://doi.org/10.1093/gji/ggy528

Pan, L., Chen, X., Wang, J., Yang, Z., & Zhang, D. (2019). Sensitivity analysis of dispersion curves of Raleigh waves with fundamental and higher modes. *Geophysical Journal International*, *216*(2), 1276–1303. https://doi.org/10.1093/gji/ggy479

Pan, Y., Gao, L., & Bohlen, T. (2021). Random-objective waveform inversion of 3D-9C shallow-seismic field data. *Journal of Geophysical Research: Solid Earth*, *126*(9), e2021JB022036. https://doi.org/10.1029/2021jb022036

Park, C. B. (2005). *Masw horizontal resolution in 2D shear-velocity (vs) mapping*. *Open-File Report* (Vol. 36). Kansas Geologic Survey. Retrieved from http://www.masw.com/files/KGS-05-04.pdf

Parsons, T., & McCarthy, J. (1996). Crustal and upper mantle velocity structure of the Salton Trough, southeast California. *Tectonics*, *15*(2), 456–471. https://doi.org/10.1029/95tc02616

Persaud, P., Ma, Y., Stock, J. M., Hole, J. A., Fuis, G. S., & Han, L. (2016). Fault zone characteristics and basin complexity in the southern Salton Trough, California. *Geology*, *44*(9), 747–750. https://doi.org/10.1130/g38033.1

Planès, T., Obermann, A., Antunes, V., & Lupi, M. (2020). Ambient-noise tomography of the Greater Geneva Basin in a geothermal exploration context. *Geophysical Journal International*, *220*(1), 370–383. https://doi.org/10.1093/gji/ggz457

Prieto, G. A., Lawrence, J. F., & Beroza, G. C. (2009). Anelastic Earth structure from the coherency of the ambient seismic field. *Journal of Geophysical Research*, *114*(B7), B07303. https://doi.org/10.1029/2008JB006067

Robinson, P. T., Elders, W. A., & Muffler, L. P. (1976). Quaternary volcanism in the Salton Sea geothermal field, Imperial Valley, California. *Geological Society of America Bulletin*, *87*(3), 347–360. https://doi.org/10.1130/0016-7606(1976)87<347:qvitss>2.0.co;2

Rodríguez Tribaldos, V., Ajo-Franklin, J., Dou, S., Lindsey, N. J., Ulrich, C., Robertson, M., et al. (2021). Surface wave imaging using distributed acoustic sensing deployed on dark fiber: Moving beyond high-frequency noise. *Distributed Acoustic Sensing in Geophysics: Methods and Applications*, 197–212.

Ryan, G. A., & Shalev, E. (2014). Seismic velocity/temperature correlations and a possible new geothermometer: Insights from exploration of a high-temperature geothermal system on Montserrat, West Indies. *Energies*, *7*(10), 6689–6720. https://doi.org/10.3390/en7106689

Santos, P. A., & Rivas, J. A. (2009). *Gravity survey contribution to geothermal exploration in El Salvador: The cases of Berlín, Ahuachapán and San Vicente Areas*. LaGeo SA de CV United Nations University Geothermal Training Program.

Sbrana, A., Lenzi, A., Paci, M., Gambini, R., Sbrana, M., Ciani, V., & Marianelli, P. (2021). Analysis of natural and power plant CO_2 emissions in the Mount Amiata (Italy) volcanic–geothermal area reveals sustainable electricity production at zero emissions. *Energies*, *14*(15), 4692. https://doi.org/10.3390/en14154692

Schimmel, M., & Paulssen, H. (1997). Noise reduction and detection of weak, coherent signals through phase weighted stacks. *Geophysical Journal International*, *130*(2), 497–505. https://doi.org/10.1111/j.1365-246x.1997.tb05664.x

Schimmel, M., Stutzmann, E., & Gallart, J. (2011). Using instantaneous phase coherence for signal extraction from ambient noise data at a local to a global scale. *Geophysical Journal International*, *184*(1), 494–506. https://doi.org/10.1111/j.1365-246x.2010.04861.x

Schmitt, A. K., & Hulen, J. B. (2008). Buried rhyolites within the active, high-temperature Salton Sea geothermal system. *Journal of Volcanology and Geothermal Research*, *178*(4), 708–718. https://doi.org/10.1016/j.jvolgeores.2008.09.001

Schölderle, F., Lipus, M., Pfrang, D., Reinsch, T., Haberer, S., Einsiedl, F., & Zosseder, K. (2021). Monitoring cold water injections for reservoir characterization using a permanent fiber optic installation in a geothermal production well in the Southern German Molasse Basin. *Geothermal Energy*, *9*(1), 1–36. https://doi.org/10.1186/s40517-021-00204-0

Schuster, G., Yu, J., Sheng, J., & Rickett, J. (2004). Interferometric/daylight seismic imaging. *Geophysical Journal International*, *157*(2), 838–852. https://doi.org/10.1111/j.1365-246x.2004.02251.x

Shapiro, N. M., & Campillo, M. (2004). Emergence of broadband Raleigh waves from correlations of the ambient seismic noise. *Geophysical Research Letters*, *31*(7). https://doi.org/10.1029/2004gl019491

Small, P., Gill, D., Maechling, P. J., Taborda, R., Callaghan, S., Jordan, T. H., et al. (2017). The SCEC unified community velocity model software framework. *Seismological Research Letters*, *88*(6), 1539–1552. https://doi.org/10.1785/0220170082

Snieder, R. (2004). Extracting the Green's function from the correlation of coda waves: A derivation based on stationary phase. *Physical Review E*, *69*(4), 046610. https://doi.org/10.1103/physreve.69.046610

Snieder, R., Miyazawa, M., Slob, E., Vasconcelos, I., & Wapenaar, K. (2009). A comparison of strategies for seismic interferometry. *Surveys in Geophysics*, *30*(4–5), 503–523. https://doi.org/10.1007/s10712-009-9069-z

Song, Z., Zeng, X., Xie, J., Bao, F., & Zhang, G. (2021). Sensing shallow structure and traffic noise with fiber-optic internet cables in an urban area. *Surveys in Geophysics*, *42*(6), 1401–1423. https://doi.org/10.1007/s10712-021-09678-w

Soyer, W., Mackie, R., Hallinan, S., Pavesi, A., Nordquist, G., Suminar, A., et al. (2018). Geologically consistent multiphysics imaging of the Darajat geothermal steam field. *First Break*, *36*(6), 77–83. https://doi.org/10.3997/1365-2397.n0102

Spica, Z. J., Nakata, N., Liu, X., Campman, X., Tang, Z., & Beroza, G. C. (2018). The ambient seismic field at Groningen Gas Field: An overview from the surface to reservoir depth. *Seismological Research Letters*, *89*(4), 1450–1466. https://doi.org/10.1785/0220170256

Takei, Y. (2002). Effect of pore geometry on V_p/V_s: From equilibrium geometry to crack. *Journal of Geophysical Research*, *107*(B2), ECV 6-1–ECV 6-12. https://doi.org/10.1029/2001jb000522

Thanassoulas, C. (1991). Geothermal exploration using electrical methods. *Geoexploration*, *27*(3–4), 321–350. https://doi.org/10.1016/0016-7142(91)90005-w

Towse, D., & Palmer, T. (1976). *Summary of geology at the ERDA–MAGMA–SDG and E geothermal test site* (Technical Report). California University; Lawrence Livermore Lab. https://doi.org/10.2172/7359119

Tyler, S. W., Selker, J. S., Hausner, M. B., Hatch, C. E., Torgersen, T., Thodal, C. E., & Schladow, S. G. (2009). Environmental temperature sensing using Raman spectra DTS fiber-optic methods. *Water Resources Research*, *45*(4), W00D23. https://doi.org/10.1029/2008wr007052

Ventosa, S., Schimmel, M., & Stutzmann, E. (2017). Extracting surface waves, hum and normal modes: Time-scale phase-weighted stack and beyond. *Geophysical Journal International*, *211*(1), 30–44. https://doi.org/10.1093/gji/ggx284

Viens, L., Bonilla, L. F., Spica, Z. J., Nishida, K., Yamada, T., & Shinohara, M. (2022). Nonlinear earthquake response of marine sediments with distributed acoustic sensing. *Geophysical Research Letters*, *49*(21), e2022GL100122. https://doi.org/10.1029/2022gl100122

Waagaard, O. H., Rønnekleiv, E., Haukanes, A., Stabo-Eeg, F., Thingbø, D., Forbord, S., et al. (2021). Real-time low noise distributed acoustic sensing in 171 km low loss fiber. *OSA Continuum*, *4*(2), 688–701. https://doi.org/10.1364/osac.408761

Walck, M. C. (1988). Three-dimensional V_p/V_s variations for the Coso Region, California. *Journal of Geophysical Research*, *93*(B3), 2047–2052. https://doi.org/10.1029/jb093ib03p02047

Walter, F., Gräff, D., Lindner, F., Paitz, P., Köpfli, M., Chmiel, M., & Fichtner, A. (2020). Distributed acoustic sensing of microseismic sources and wave propagation in glaciated terrain. *Nature Communications*, *11*(1), 1–10. https://doi.org/10.1038/s41467-020-15824-6

Wang, X., Williams, E. F., Karrenbach, M., Herráez, M. G., Martins, H. F., & Zhan, Z. (2020). Rose Parade seismology: Signatures of floats and bands on optical fiber. *Seismological Research Letters*, *91*(4), 2395–2398. https://doi.org/10.1785/0220200091

Wapenaar, K. (2004). Retrieving the elastodynamic Green's function of an arbitrary inhomogeneous medium by cross correlation. *Physical Review Letters*, *93*(25), 254301. https://doi.org/10.1103/physrevlett.93.254301

Ward, P. L. (1972). Microearthquakes: Prospecting tool and possible hazard in the development of geothermal resources. *Geothermics*, *1*(1), 3–12. https://doi.org/10.1016/0375-6505(72)90003-x

Wathelet, M., Jongmans, D., & Ohrnberger, M. (2004). Surface-wave inversion using a direct search algorithm and its application to ambient vibration measurements. *Near Surface Geophysics*, *2*(4), 211–221. https://doi.org/10.3997/1873-0604.2004018

Wei, S., Avouac, J.-P., Hudnut, K. W., Donnellan, A., Parker, J. W., Graves, R. W., et al. (2015). The 2012 Brawley swarm triggered by injection-induced aseismic slip. *Earth and Planetary Science Letters*, *422*, 115–125. https://doi.org/10.1016/j.epsl.2015.03.054

Wei, S., Helmberger, D., Owen, S., Graves, R. W., Hudnut, K. W., & Fielding, E. J. (2013). Complementary slip distributions of the largest earthquakes in the 2012 brawley swarm, imperial valley, California. *Geophysical Research Letters*, *40*(5), 847–852. https://doi.org/10.1002/grl.50259

Williams, C., Reed, M. J., DeAngelo, J., & Galanis, S. P., Jr. (2009). Quantifying the undiscovered geothermal resources of the United States. In *Geothermal Resources Council 2009 Annual Meeting* (Vol. 33).

Williams, C., Reed, M. J., Galanis, S., Jr., & DeAngelo, J. (2007). The USGS national geothermal resource assessment: An update. In *Geothermal Resources Council-Annual Meeting of the Geothermal Resources Council 2007* (Vol. 31, pp. 99–104).

Williams, C., Reed, M. J., Mariner, R. H., DeAngelo, J., & Galanis, S. P. (2008). *Assessment of moderate-and high-temperature geothermal resources of the United States* (Technical Report). Geological Survey. Retrieved from http://pubs.usgs.gov/fs/2008/3082

Williams, E. F., Fernández-Ruiz, M. R., Magalhaes, R., Vanthillo, R., Zhan, Z., González-Herráez, M., & Martins, H. F. (2021). Scholte wave inversion and passive source imaging with ocean-bottom DAS. *The Leading Edge*, *40*(8), 576–583. https://doi.org/10.1190/tle40080576.1

Xia, J., Miller, R. D., & Park, C. B. (1999). Estimation of near-surface shear-wave velocity by inversion of Raleigh waves. *Geophysics*, *64*(3), 691–700. https://doi.org/10.1190/1.1444578

Xia, J., Miller, R. D., Xu, Y., Luo, Y., Chen, C., Liu, J., et al. (2009). High-frequency Raleigh-wave method. *Journal of Earth Science*, *20*(3), 563–579. https://doi.org/10.1007/s12583-009-0047-7

Xia, J., Xu, Y., Chen, C., Kaufmann, R. D., & Luo, Y. (2006). Simple equations guide high-frequency surface-wave investigation techniques. *Soil Dynamics and Earthquake Engineering*, *26*(5), 395–403. https://doi.org/10.1016/j.soildyn.2005.11.001

Xia, J., Xu, Y., Luo, Y., Miller, R. D., Cakir, R., & Zeng, C. (2012). Advantages of using multichannel analysis of Love waves (MALW) to estimate near-surface shear-wave velocity. *Surveys in Geophysics*, *33*(5), 841–860. https://doi.org/10.1007/s10712-012-9174-2

Yang, Y., Zhan, Z., Shen, Z., & Atterholt, J. (2022). Fault zone imaging with distributed acoustic sensing: Surface-to-surface wave scattering. *Journal of Geophysical Research: Solid Earth*, *127*(6), e2022JB024329. https://doi.org/10.1029/2022jb024329

Younker, L. W., Kasameyer, P. W., & Tewhey, J. D. (1982). Geological, geophysical, and thermal characteristics of the Salton Sea Geothermal Field, California. *Journal of Volcanology and Geothermal Research*, *12*(3–4), 221–258. https://doi.org/10.1016/0377-0273(82)90028-2

Zehner, R. E., Tullar, K. N., & Rutledge, E. (2012). Effectiveness of 2-meter and geoprobe shallow temperature surveys in early stage geothermal exploration. *GRC Transaction*, *36*, 835–841.

Zeng, X., Lancelle, C., Thurber, C., Fratta, D., Wang, H., Lord, N., et al. (2017). Properties of noise cross-correlation functions obtained from a distributed acoustic sensing array at Garner Valley, California. *Bulletin of the Seismological Society of America*, *107*(2), 603–610. https://doi.org/10.1785/0120160168

Zeng, X., & Ni, S. (2010). A persistent localized microseismic source near the Kyushu Island, Japan. *Geophysical Research Letters*, *37*(24), 8–13. https://doi.org/10.1029/2010GL045774

Zeng, X., Thurber, C. H., Wang, H. F., Fratta, D., & Feigl, K. L. (2021). High-resolution shallow structure at Brady Hot Springs using ambient noise tomography (ANT) on a trenched distributed acoustic sensing (DAS) array. *Distributed Acoustic Sensing in Geophysics: Methods and Applications*, 101–110.

Zhan, Z. (2020). Distributed acoustic sensing turns fiber-optic cables into sensitive seismic antennas. *Seismological Research Letters*, *91*(1), 1–15. https://doi.org/10.1785/0220190112

Zhang, C., Yao, H., Liu, Q., Zhang, P., Yuan, Y. O., Feng, J., & Fang, L. (2018). Linear array ambient noise adjoint tomography reveals intense crust-mantle interactions in North China Craton. *Journal of Geophysical Research: Solid Earth*, *123*(1), 368–383. https://doi.org/10.1002/2017jb015019

Zhou, C., Xia, J., Pang, J., Cheng, F., Chen, X., Xi, C., et al. (2021). Near-surface geothermal reservoir imaging based on the customized dense seismic network. *Surveys in Geophysics*, *42*(3), 673–697. https://doi.org/10.1007/s10712-021-09642-8

Zhu, T., & Stensrud, D. J. (2019). Characterizing thunder–induced ground motions using fiber-optic distributed acoustic sensing array. *Journal of Geophysical Research: Atmospheres*, *124*, (23), 810–823. https://doi.org/10.1029/2019JD031453

Zucca, J., Hutchings, L., & Kasameyer, P. (1994). Seismic velocity and attenuation structure of the Geysers geothermal field, California. *Geothermics*, *23*(2), 111–126. https://doi.org/10.1016/0375-6505(94)90033-7